Parametric Analysis of Pitch Angle Scattering and Losses of Relativistic Electrons by Oblique EMIC Waves

Miroslav Hanzelka [1,2*], Wen Li [1], and Qianli Ma [1,3]

[1] *Center for Space Physics, Boston University, Boston, MA, USA*
[2] *Department of Space Physics, Institute of Atmospheric Physics of the Czech Academy of Sciences, Prague, Czech Republic*
[3] *Department of Atmospheric and Oceanic Sciences, UCLA, Los Angeles, CA, USA*

Correspondence*:
Center for Space Physics, Boston University, 725 Commonwealth Avenue, Boston, MA 02215, USA
mirekhanzelka@gmail.com

ABSTRACT

We analyze the effects of electromagnetic ion cyclotron (EMIC) waves on relativistic electron scattering and losses in the Earth's outer radiation belt. The EMIC emissions are commonly observed in the inner magnetosphere and are known to reach high amplitudes, causing significant pitch angle changes in $>$1 MeV electrons via cyclotron resonant interactions. We run test-particle simulations of electrons streaming through helium-band waves with different amplitudes and wave normal angles and assess the sensitivity of advective and diffusive scattering behavior to these two parameters, including the possibility of very oblique propagation. The numerical analysis confirms the importance of harmonic resonances for oblique waves, and the very oblique waves are observed to efficiently scatter both co-streaming and counter-streaming electrons. However, strong finite Larmor radius effects limit the scattering efficiency at high pitch angles. Recently discussed force bunching effects and associated strong positive advection at low pitch angles are, surprisingly, shown to cause no decrease in the phase space density of precipitating electrons, and it is demonstrated that the transport of electrons into the loss cone balances out the scattering out of the loss cone. In the case of high-amplitude obliquely propagating waves, weak but nonnegligible losses are detected well below the minimum resonant energy, and we identify them as the result of nonlinear fractional resonances. Simulations and theoretical analysis suggest that these resonances might contribute to subrelativistic electron precipitation but are likely to be overshadowed by nonresonant effects.

Keywords: electron scattering, EMIC waves, nonlinear wave-particle interactions, test-particle simulation, radiation belts, fractional resonance, loss cone, electron precipitation

1 INTRODUCTION

Electromagnetic ion cyclotron (EMIC) waves are naturally occurring electromagnetic emissions in Earth's magnetosphere generated by unstable anisotropic hot ion populations (Kennel and Petschek, 1966; Anderson et al., 1996). Each ion component of the space plasma has a corresponding EMIC frequency band located below the gyrofrequency of the ion, with the hydrogen band (H+) and helium band (He+) being the most commonly observed (Min et al., 2012; Meredith et al., 2014; Saikin et al., 2015; Wang et al., 2017b; Jun et al., 2021). In the outer radiation belt, the wave frequencies in the near-equatorial source (Loto'aniu et al., 2005; Allen et al., 2015) fall mainly into the Pc1 range $0.2–5\,\mathrm{Hz}$ (Saito, 1969; Usanova et al., 2012). Initially generated in the left-handed mode, the waves may convert to the right-handed mode at higher latitudes (Rauch and Roux, 1982; Perraut et al., 1984; Kim and Johnson, 2016). These polarized waves can scatter relativistic electrons (kinetic energies E_k around $1\,\mathrm{MeV}$ and larger) in pitch angle α through cyclotron resonant interactions (Summers et al., 1998; Horne and Thorne, 1998), which leads to significant losses of radiation belt electrons to the atmosphere (Thorne and Kennel, 1971; Usanova et al., 2014; Clilverd et al., 2015; Kurita et al., 2018; Li and Hudson, 2019).

During geomagnetically active times, EMIC waves at lower L-shells ($L < 6$) can reach peak magnetic field amplitudes B_w above one percent of the background magnetic field strength B_0 (Meredith et al., 2003; Engebretson et al., 2015). Trajectories of particles resonating with strong waves experience large perturbations, and a variety of associated nonlinear effects appear (Karpman, 1974; Artemyev et al., 2018; Grach et al., 2022). Phase-trapping of ions in the wave potential leads to nonlocal transport to higher pitch angles and the formation of phase space density (PSD) holes in the gyrophase space (Omura et al., 2010; Shoji et al., 2021), while phase-trapped electrons experience a decrease in pitch angle (Omura and Zhao, 2012; Zheng et al., 2019). At $\alpha \approx 0^\circ$, the force-bunched electrons are transported predominantly to higher pitch angles; Bortnik et al. (2022) proposed that this nonlinear effect may result in precipitation blocking due to the removal of electrons from the loss cone. Below the fundamental cyclotron resonance energy, nonresonant scattering by amplitude-modulated waves takes place and may extend the energy range of precipitating electrons down to hundreds of keV (Chen et al., 2016; An et al., 2022).

When the wave normal angle θ_k (WNA) of EMIC waves increases and the propagation becomes oblique, finite Larmor radius effects enable interaction with higher cyclotron harmonics. Wang et al. (2017a) studied the interaction of electrons with moderately oblique monochromatic EMIC waves through nonlinear test-particle simulations and quasilinear diffusive modeling. They have shown that with increasing θ_k, harmonic resonances at ultrarelativistic energies can lead to significant scattering loss, while the fundamental resonance becomes weaker for oblique waves. Lee et al. (2018) analyzed WNA and ellipticity of a set of EMIC waves detected by Van Allen Probe A, ran test-particle simulations of electron interaction with very powerful and oblique EMIC waves, and highlighted the complexity of pitch-angle evolution due to higher-order resonance with the elliptically polarized wave. They also emphasized the advective aspects of nonlinear scattering and noted the importance of ellipticity and WNA distributions in modeling the radiation belt electron transport.

In this paper, we perform test-particle simulations of nonlinear electron interactions with quasiparallel and very oblique monochromatic EMIC waves, with the overall goal to describe the dependence of advection, diffusion, and subsequent particle losses on the wave amplitude and wave normal angle – special attention is given to the PSD evolution at low pitch angles. After describing the simulation setup in Section 2, we analyze the average and standard deviation of equatorial pitch angle changes and show that for very oblique waves and discuss the influence of higher harmonics on advection and diffusion 3.1. In Section 3.2, we demonstrate through Liouville mapping of phase space density in backward-in-time simulations that the force-bunching effects at low pitch angles are balanced out by transport from higher pitch angles and that there is no precipitation blocking in the sense of decreasing precipitating electrons PSD below the trapped PSD. Section 3.3 describes fractional resonances, a type of resonance acting below the fundamental resonance energy, and considers their effects on subrelativistic electrons. A summary of the most salient results and the discussion of the impacts of our findings on radiation belt electron modeling can be found in Section 4.

2 METHODS AND SIMULATION SETUP

Before choosing representative wave and plasma parameters for our particle simulation, we must first consider which quantities can influence the behavior of resonant electrons. Wave amplitude B_w controls the transition from quasilinear to nonlinear interaction, and wave normal angle θ_k is related to the perpendicular component of the wave vector and associated harmonic resonances. Varying the values of B_w or θ_k leads to major qualitative changes in the resonant behavior; therefore, they are the essential parameters in our simulation. We choose four values of wave normal angle $\{5°, 45°, 70°, 80°\}$ to cover quasiparallel, moderately oblique, and very oblique wave propagation. The WNA values are combined with three values of amplitude $\{100\,\mathrm{pT}, 400\,\mathrm{pT}, 1.6\,\mathrm{nT}\}$, which approximately correspond to $B_\mathrm{w}/B_\mathrm{0eq}$ ratios of $\{0.04\%, 0.16\%, 0.64\%\}$ for equatorial field strength $B_\mathrm{0eq} = 248\,\mathrm{nT}$ at $L = 5$. This choice of L-shell is consistent with regions of enhanced EMIC wave activity identified by Meredith et al. (2014) and Jun et al. (2021) in spacecraft measurements during active geomagnetic conditions.

There are also several parameters that influence the value of the minimum resonant energy, which is given by the formula

$$E_\mathrm{Rmin} = mc^2 \left(\frac{n\omega\Omega_\mathrm{e} - k_\parallel c\sqrt{n^2\Omega_\mathrm{e}^2 + k_\parallel^2 c^2 - \omega^2}}{\omega^2 - k_\parallel^2 c^2} - 1 \right) , \tag{1}$$

where m is the electron mass, c is the speed of light, $k_\parallel$ is the component of wave vector parallel to $\boldsymbol{B_0}$, ω is the wave frequency, Ω_e is the local electron gyrofrequency, and n is an integer determining the resonance harmonic (positive/negative for electrons streaming against/along a right/left-handed wave). The energy E_Rmin is dependent on the normalized frequency ω/Ω_e, and through the cold plasma dispersion relation $k(\omega)$, it also depends on the electron plasma frequency ω_pe and the concentration of ions. These dependencies are evaluated and plotted in Figure 1, where we plot E_Rmin with $n = -1$ for a monochromatic left-handed EMIC wave propagating from the magnetic equator along a dipole field line up to magnetic latitude $\lambda_\mathrm{m} = 30°$. We consider high ($\omega_\mathrm{pe0}/\Omega_\mathrm{e0} = 15$) as well as low ($\omega_\mathrm{pe0}/\Omega_\mathrm{e0} = 5$) density at the equator, and we compare the high concentrations of ions ($n_\mathrm{p}/n_\mathrm{e} = 0.77$, $n_\mathrm{He}/n_\mathrm{e} = 0.2$, $n_\mathrm{O}/n_\mathrm{e} = 0.03$), which was used in the simulations of Jordanova et al. (2008) and Bortnik et al. (2022), with lower concentrations ($n_\mathrm{p}/n_\mathrm{e} = 0.99$, $n_\mathrm{He}/n_\mathrm{e} = 0.005$, $n_\mathrm{O}/n_\mathrm{e} = 0.005$). Latitudinal dependence of density follows the Denton et al. (2002) formula $n_\mathrm{e} = n_\mathrm{e0}(\cos\lambda_\mathrm{m})^{-2a}$, with $a = 0.5$ in the high-density case and $a = 1.0$ in the low-density case (and the relative ion concentrations remain constant). We observe that changes to the density, ion concentration, and frequency band manifest mostly through a rescaling of E_Rmin. Therefore, we limit our investigations to the helium band and choose the higher values of density ($\omega_\mathrm{pe0}/\Omega_\mathrm{e0} = 15 \sim n_\mathrm{e0} = 134\,\mathrm{cm}^{-3}$) and ion concentrations, in agreement with the observations of Meredith et al. (2014) and Horwitz et al. (1981). The wave frequency is set to $\omega/\Omega_\mathrm{He0} = 0.80 \sim 0.76\,\mathrm{Hz}$, a slightly higher value that allows the waves to reach higher latitudes before experiencing the polarization reversal.

Apart from the strong interaction near resonant energies, electrons can also experience nonresonant scattering due to wave amplitude gradients (Chen et al., 2016) or, equivalently, due to the spectral broadening of amplitude-modulated waves (An et al., 2022). To simplify our analysis, we suppress the nonresonant scattering by introducing a slow and smooth amplitude change at the edges of the wave packet. This is done by multiplying the wave envelope by a half-period of the $\cos^2$ function, with a field-aligned distance from the minimum to the maximum of the function set to $h = 2200\,\mathrm{km}$. The envelope shape is plotted in Figure 2a. The packet ends at a latitude where the normalized frequency reaches $\omega/\Omega_{\mathrm{O}} = 1.25$. At this frequency, the helium wave is already right-handed, and the resonant energy of very oblique waves rapidly increases (Stix, 1992).

The test-particle simulation method is based on the solution of the Lorentz force law by a relativistic Boris algorithm with a phase angle correction, as described, e.g., by Zenitani and Umeda (2018). The components of the electromagnetic wave field are defined according to the analysis of elliptically polarized waves presented in Omura et al. (2019); see also Equations (5)–(8) and (12)–(17) in Appendix A. Wave packet motion can be neglected on short timescales since the group velocity of EMIC waves is much smaller than the velocity of relativistic electrons. In forward-in-time simulations, the particles start either at the equator and propagate until they reach the end of the wave packet (or their mirror point) or they start at the end of the wave packet and propagate back to the equator. Mirroring particles are not allowed to return to the equator so that we can separate the resonant effects experienced by co-streaming and counter-streaming electrons. In both cases, the initial particle energy is spaced logarithmically from $900\,\mathrm{keV}$ to $30\,\mathrm{MeV}$ with 96 bins, initial pitch angles go from $0°$ to $90°$ (or $180°$ to $90°$ for counter-streaming electrons) with 90 linear steps, and the initial gyrophases φ uniformly cover the full $360°$ angle with 72 steps. Note that the grid boundaries in the $(E_{\mathrm{k}}, \alpha, \varphi)$ space represent bin edges. In backward-in-time simulations, the pitch angle range is limited to $0°$ to $20°$ (or $180°$ to $160°$ for counter-streaming electrons) with 90 linear steps, providing increased resolution of the loss cone ($\alpha_{\mathrm{loss}} = 3.6°$ at the equator and $6.1°$ at the end of the packet). The time step of the Boris solver is adaptive and always stays at 128 steps per local electron gyroperiod.

The backward-in-time simulations are used to map the phase space density of an initial, unperturbed distribution to the final state and assess the PSD evolution due to resonant interactions (Nunn and Omura, 2015; Hanzelka et al., 2021). We assume that the initial hot (relativistic) distribution is in the form of a sum of subtracted bi-Maxwellian distributions that preserves phase space density along adiabatic trajectories (Summers et al., 2012; Omura, 2021). At a distance h, this distribution can be written for relativistic momenta $u_\parallel = \gamma v_\parallel$ and $u_\perp = \gamma v_\perp$ as

$$f(h, u_\parallel, u_\perp) = \sum_{i=1}^{N} f_i(h, u_\parallel, u_\perp) \tag{2}$$

with

$$\begin{aligned} f_i(h, u_\parallel, u_\perp) = & \frac{n_{\mathrm{he0}i}}{(2\pi)^{3/2} U_{\mathrm{t}\parallel i} U_{\mathrm{t}\perp i}^2 (1-\rho_i\beta_i)} \exp\left(-\frac{u_\parallel^2}{2U_{\mathrm{t}\parallel i}^2}\right) \times \\ & \times \left[\exp\left(-\left(\frac{1 - B_{0\mathrm{eq}}/B_0(h)}{2B_0(h)U_{\mathrm{t}\perp i}^2} + \frac{B_{0\mathrm{eq}}}{2B_0(h)U_{\mathrm{t}\perp i}^2}\right) u_\perp^2\right) - \right. \\ & \left. - \rho_i \exp\left(-\left(\frac{1 - B_{0\mathrm{eq}}/B_0(h)}{2B_0(h)U_{\mathrm{t}\parallel i}^2} + \frac{B_{0\mathrm{eq}}}{2\beta_i B_0(h)U_{\mathrm{t}\parallel i}^2}\right) u_\perp^2\right)\right] . \end{aligned} \tag{3}$$

We set $N = 5$ and choose the following values of distribution parameters: loss cone width $\beta_i = 0.5\,\forall i$, loss cone height $\beta_i = 1.0\,\forall i$, parallel and perpendicular thermal momenta $U_{\mathrm{t}\|i}/c = U_{\mathrm{t}\perp i}/c = \{0.2, 0.5, 1.0, 2.5, 9.0\}$, and hot electron densities $n_{\mathrm{he}0i} = \{2.2, 0.22, 0.022, 0.0022, 2.2 \cdot 10^{-7}\}\,\mathrm{cm}^{-3}$. PSD inside the loss cone is set to zero for all values of h. The equatorial distribution is plotted in Figure 2b in the $(E_\mathrm{k}, \alpha_\mathrm{ini})$ space. The energy profile up to $10\,\mathrm{MeV}$ is constructed to loosely follow the Van Allen Probes measurements analyzed by Zhao et al. (2019); however, the energy distribution is of little importance for EMIC-electron resonance since the acceleration caused by this interaction is negligible (Summers et al., 1998). Line plots of pitch angle distributions for several initial energies are presented in Figure 2c. Although each component of the initial distribution has a zero temperature anisotropy $A_\mathrm{t} = U^2_{\mathrm{t}\perp}/U^2_{\mathrm{t}\|} - 1$, the relativistic pitch angle anisotropy (Xiao et al., 1998) can be large due to the subtraction in the PSD distribution model. This model is consistent with the assumption that previous weaker wave-particle interactions already eroded the pitch angle profile.

3 RESULTS

3.1 Advection and Diffusion

When studying the nonlinear interactions between plasma waves and charged particles, it is illustrative to start by inspecting individual trajectories. In Figure 3, we plot the spatial evolution of the equatorial pitch angle for electrons propagating through a high-amplitude ($B_\mathrm{w}/B_{0\mathrm{eq}} = 0.0064$) moderately oblique ($\theta_\mathrm{k} = 45^\circ$) EMIC wave. The equatorial minimum resonance energy for this wave is $E_\mathrm{Rmin} \approx 3.3\,\mathrm{MeV}$ for $n = \pm 1$ and $E_\mathrm{Rmin} \approx 7.1\,\mathrm{MeV}$ for $n = \pm 2$. Particles starting at the equator with initial pitch angle $\alpha = 0.5^\circ$ and energies $E_\mathrm{k} = 3.95\,\mathrm{MeV}$ experience a significant increase in equatorial pitch angle $\Delta\alpha_\mathrm{eq} \approx 11^\circ$ due to the $n = -1$ resonance, with almost no dependence on the initial gyrophase (Figure 3a). This is the advective behavior caused by force bunching, as previously described by Grach and Demekhov (2020). Particles starting at larger pitch angles ($\alpha_\mathrm{eq} = 29.5^\circ$, Figure 3b) experience a large spread in α_eq across the gyrophases, exhibiting a predominantly diffusive behavior. The asymmetry in $\Delta\alpha_\mathrm{eq}$ towards lower values is caused by phase locking of φ to the wave phase ψ, but the particles never become fully phase-trapped in this particular case. In Figure 3c, we increase the initial energy to $E_\mathrm{k} = 8.51\,\mathrm{MeV}$ and observe that particles first undergo scattering due to the $n = -2$ harmonic resonance and then encounter the $n = -1$ resonance at latitudes from 11° to 16°, resulting in pitch-angle diffusion.

Figures 3d–3f show particle trajectories of electrons starting at the end of the wave packet and streaming against the wave. Here, resonant interaction is enabled by the right-handed component of the elliptically polarized wave. Keeping the initial energies and initial equatorial pitch angles similar to the co-streaming case, we observe that the advective and diffusive effects of the $n = 1$ resonance are comparable to the $n = -1$ resonance. However, the maximum change in pitch angle is smaller, and the phase-locking effect does not appear. In the case with $E_\mathrm{k} = 8.51\,\mathrm{MeV}$, the counter-streaming particles first encounter the stronger $n = 1$ resonance, and the weaker $n = 2$ resonance has then only a little effect on the spread in $\Delta\alpha_\mathrm{eq}$.

To evaluate the pitch angle evolution of relativistic electrons across all initial pitch angles and energies, we introduce two statistical measures: the average $\langle\Delta\alpha_\mathrm{eq}\rangle_\varphi$ (first central moment), which is related to the advection coefficient, and the standard deviation $\sigma_\varphi(\alpha_\mathrm{eq})$ (second central moment), which is related to the diffusion coefficient. We intentionally eschew the standard advection and diffusion coefficients (Zheng et al., 2019) as they are often bounce-averaged in practical applications, while we do not let the particles finish the half-bounce, which is to separate between $n > 0$ and $n < 0$ resonances. The average change in equatorial pitch angle for co-streaming particles is plotted in Figure 4 in $(\alpha_{\mathrm{ini}}, E_{\mathrm{k}})$ coordinates, with each plot corresponding to one of the 3 combinations of wave amplitude and wave normal angle. Starting with quasiparallel propagation ($\theta_{\mathrm{k}} = 5°$, Figures 4a–4c), we first note the different scales of color bars, which have a range of $\pm \max_{(\alpha_{\mathrm{ini}}, E_{\mathrm{k}})} |\langle \Delta\alpha_{\mathrm{eq}} \rangle_{\varphi}|$ separately for each plot. An outstanding feature, high positive advection, appears at low pitch angles near the $n = -1$ resonance, confirming the force-bunching effects observed on trajectories in Figure 3a. Another prominent feature is the two red (positive) and blue (negative) curved stripes that follow the dependence of $n = -1$ resonant energy on pitch angle. For the case with the largest wave amplitude (Figure 4c), the negative advection at higher pitch angles dominates over the positive one, indicating significant nonlinear phase-trapping effects.

Interaction with oblique waves (Figures 4d–4l) introduces some new effects. First, we may notice the alternating blue and red vertical lines at high pitch angles, with almost no dependence on energy. These are the result of nonresonant oscillations induced by the parallel component of the wave field, and they would almost disappear if the particles were allowed to bounce back to the equator – the lines are not relevant for our analysis of the cyclotron resonance and will be omitted in the following presentation. Harmonic resonances become visible at higher amplitudes, adding new pairs of positive and negative advective stripes along the corresponding resonance energy curves. However, as the wave normal angle increases, advective effects disappear at higher pitch angles; for $\theta_{\mathrm{k}} = 80°$, the average change in pitch angle becomes negligible for particles with $\alpha_{\mathrm{ini}} > 30°$. Moreover, a fine stripe structure traversing the resonant energy curves appears in the high-amplitude plots. These new effects will be explained below when discussing the diffusive behavior, where their origin becomes more apparent.

The standard deviation in the equatorial pitch angle of co-streaming particles is plotted in Figure 5, following the panel format of Figure 4. The color bars of each individual panel go from zero to $\max_{(\alpha_{\mathrm{ini}}, E_{\mathrm{k}})} \sigma_{\varphi}(\alpha_{\mathrm{eq}})$. Starting again with the quasiparallel propagation ($\theta_{\mathrm{k}} = 5°$, Figures 5a–5c), we can see the suppressed diffusion at low pitch angles, consistent with the lack of spread in pitch angles observed in the particle trajectories (Figure 3a). The largest values of $\sigma_{\varphi}(\alpha_{\mathrm{eq}})$ are localized along the resonance energy curve, with slight changes appearing for $B_{\mathrm{w}} = 1.6\,\mathrm{nT}$ at higher pitch angles, where and phase-trapping and bunching effects may enhance or decrease the standard deviation. In the oblique case, diffusion at higher pitch angles gets weaker with growing wave normal angle. Unlike in the analysis of advection, we detect a clear structure of maxima and minima along each resonant curve, which is related to the zeros of Bessel functions that arise in the derivation of harmonic resonances (see Appendix A, Equations (9)–(11) and (20)–(22)). The fine structure appearing in the energy range of harmonic resonances is now also more evident, especially in the high-amplitude case (Figures 5f, 5i, and 5l). By inspecting trajectory plots, its origin can be traced to multiresonance interactions, when particles phase-organized by the resonance of order $|n|$ at lower latitudes experience a $|n-1|$ resonance at higher latitudes. Notice that the fine structure is also present in the quasiparallel case, showing us that the harmonic resonances are important even at WNA as low as $\theta_{\mathrm{k}} = 5°$.

Concerning the strength of diffusion at lower pitch angles, the test-particle simulations show a decreasing trend in $\sigma_{\varphi}(\alpha_{\mathrm{eq}})$ with increasing WNA at energies close to the $n = -1$ resonance. Harmonic resonances get stronger compared to the fundamental, but the overall diffusion at higher energies does not change much because the increased strength of near-equatorial harmonic interaction is compensated by the weaker fundamental resonance encountered at higher latitudes. An exception is the extreme ultrarelativistic energies ($E_{\mathrm{k}} \gtrsim 15\,\mathrm{MeV}$), where the interaction with very oblique waves causes slightly stronger diffusion (Figures 5i and 5l). This behavior will impact the precipitation into the loss cone, as discussed in the next section.

3.2 Phase Space Density near Loss Cone

The scattering effects analyzed in Section 3.1 transport particles into the loss cone and contribute thus to the atmospheric precipitation of relativistic electrons. As described in Section 2, we trace particles back in time from the end of the wave packet to the equator and map the PSD values of a known equatorial distribution along particle trajectories to the starting point. The resulting PSD distributions at the end of the packet are plotted in Figure 6 in the $(\alpha_{\mathrm{end}}, E_{\mathrm{k}})$ space, where α_{end} is the initial pitch angle value in the sense of backward-in-time propagation. Since the number density of relativistic electrons in our model is not scaled to any specific spacecraft observation, we keep normalized phase space density units $c^{-6}\Omega_{\mathrm{e0}}^{3}$ used in the simulation code.

The quasiparallel EMIC wave manages to completely fill the loss cone near fundamental resonant energy when its amplitude is set to $B_{\mathrm{w}} = 400\,\mathrm{pT}$ (Fig. 6b). Increasing the amplitude to $B_{\mathrm{w}} = 1.6\,\mathrm{nT}$ extends the range of energies with complete loss cone filling up to $10\,\mathrm{MeV}$ (Fig. 6c). There are several noteworthy features to this strongly perturbed PSD distribution. First, we observe that particles near $E_{\mathrm{k}} = 13\,\mathrm{MeV}$ reach deeper into the loss cone, a feature not seen in the low-amplitude wave precipitation profile. This irregularity arises from the fast polarization reversal experienced by quasiparallel waves, which abruptly stops the resonant interaction – mild oscillations in $\sigma_{\varphi}(\alpha_{\mathrm{eq}})$ across energy were seen in the top left corners of Figure 5a–5c, but the effect on precipitation becomes clear only for strong waves. Second, the energy profile of trapped particles immediately above α_{loss} has a local maximum near the fundamental resonance – this peak appears due to pitch angle anisotropy when particles from high PSD regions at higher pitch angles undergo scattering towards lower pitch angles. Third, the pitch angle distribution at energies from $3\,\mathrm{MeV}$ to $10\,\mathrm{MeV}$ is flattened, signifying a marked decrease in pitch angle anisotropy. And fourth, as a consequence of the third point, there is no apparent precipitation blocking – that is, phase space density inside the loss cone reaches the value of trapped particle PSD.

The lack of precipitation blocking contradicts the predictions of Bortnik et al. (2022) and may seem counterintuitive, especially after seeing the strong upward advection at low pitch angles in Figure 4c. To explain this observation, we can consider the consequences of Liouville's theorem (i.e., constancy of PSD along phase space trajectories), which is known to hold in the Hamiltonian system of charged particles and electromagnetic waves constituting a Vlasovian plasma (Ichimaru, 2004). Assume that a state has been reached where the PSD of precipitating and trapped electrons are equal at a certain energy. Because EMIC waves cannot efficiently accelerate electrons and change their energy, the PSD along trajectories will always be the same. Therefore, no amount of force bunching or other nonlinear effects can disturb the uniform pitch angle distribution. If the PSD in the loss cone were initially higher than outside, the EMIC-induced scattering would mix the distribution and restore uniformity, decreasing thus the precipitating PSD, but it would not push it below the value of trapped PSD. Nonuniformity along the field line could complicate the argument if a broader range of $v_{\parallel}$ would be considered, but the spread in $v_{\parallel}$ at low pitch angles at a fixed energy level is negligible. The seeming discrepancy between backward-in-time PSD mapping and the transport coefficients from Section 3.1 can be resolved by considering the initial distributions of particles in the forward simulation. A uniform distribution in $(\alpha, E_{\mathrm{k}}, \varphi)$ is not uniform in (v_x, v_y, v_z); consequently, the number of particles per unit velocity space volume in the forward simulation is much higher at lower pitch angles than at higher pitch angles. Symbolically, we can write the unit volume as (working in a nonrelativistic setting for simplicity)

$$\mathrm{d}V = \mathrm{d}v_x \mathrm{d}v_y \mathrm{d}v_z = m^{-3/2}\sqrt{2E_{\mathrm{k}}}\sin\alpha\,\mathrm{d}E_{\mathrm{k}}\,\mathrm{d}\varphi\,. \tag{4}$$

The $\sin\alpha$ term in the Jacobian expresses the smallness of velocity space volume near $\alpha = 0$. Therefore, the few test particles scattered into the loss cone can have the same weight as all the force-bunched particles escaping from the loss cone.

The effect of increasing obliquity on the PSD evolution displayed in Figures 6d–6l agrees with the analysis of diffusion from Section 3.1. The loss cone is only partially filled near the fundamental resonance energy for waves with $B_\mathrm{w} = 400\,\mathrm{pT}$, and the range of complete loss cone filling with $B_\mathrm{w} = 1.6\,\mathrm{nT}$ becomes narrower with increasing θ_k. The penetration of nonzero PSD into the loss cone at higher energies turns out to be mostly independent of wave normal angle, except for ultrarelativistic energies, where the very oblique waves show larger increases in precipitating PSD. The jagged boundary between finite and zero values of PSD in the case of strong, oblique waves (mainly Figures 6i and 6l) comes from the fine multiresonance structure observed in corresponding diffusion plots in Figures 5i and 5l. The weak losses near half of the fundamental resonance energy are related to nonlinear fractional resonances, which will be analyzed in depth in Section 3.3. Finally, we note that the rapid decrease of $\sigma_\varphi(\alpha_\mathrm{eq})$ with rising WNA at higher pitch angles is not reflected in the PSD perturbations after a single quarter bounce but might become important after multiple bounces due to the weak transport of particles from high-density regions of the initial anisotropic distribution.

So far, we have investigated electron scattering and related losses for propagation along the wave. However, as indicated by Figures 3d–3f, counter-streaming particles are also efficiently scattered by oblique EMIC waves, and significant particle losses are to be expected. In Figure 7, we plot the quantities $\langle\Delta\alpha_\mathrm{eq}\rangle_\varphi$, $\sigma_\varphi(\alpha_\mathrm{eq})$, and f for electrons streaming against the medium-amplitude wave ($B_\mathrm{w} = 400\,\mathrm{pT}$) with oblique wave vectors. The quasiparallel case is omitted because the right-handed wave component is negligible until the polarization crossover at higher latitudes is reached, where the resonant energies are already near the upper limit of our E_k range. The first thing to notice is that the forward-in-time propagating particles start away from the equator and have a limited range of equatorial pitch angles; therefore, the resonance energy curves appear stretched in the $(\alpha_\mathrm{end}, E_\mathrm{k})$ space. Unlike in the co-streaming case, the advection and diffusion caused by fundamental resonance grow with increasing WNA because the polarization is becoming more linear and the right-handed wave component is getting larger. This behavior is reflected in the PSD plots, where the precipitating particles can travel deeper into the loss cone when interacting with very oblique waves. For $\theta_\mathrm{k} = 80^\circ$, the advection and diffusion (and, as a consequence, the electron losses) become comparable to the co-streaming case, showing the importance of $n > 0$ resonances for analysis for relativistic electron precipitation by oblique EMIC waves.

3.3 Nonlinear Fractional Resonances

In the discussion of Figures 6i and 6l, we mentioned the surprising detection electron scattering into loss cone at energies $E_\mathrm{k} \approx 2\,\mathrm{MeV}$, far below the fundamental resonance energy. These losses cannot have origin in nonresonant scattering because we use a smooth amplitude distribution along h, and also because the nonresonant scattering would show as a broadening of the fundamental resonance and not as a separate peak in energy profile (An et al., 2022). Trajectories of particles with energies $E_\mathrm{k} = 1.83\,\mathrm{MeV}$ and $E_\mathrm{k} = 2.12\,\mathrm{MeV}$ propagating along the high-amplitude wave with $\theta_\mathrm{k} = 70^\circ$ (Figures 8a and 8b) reveal a spread in α_eq that does not disappear even after the particles leave the wave field. This spread is somewhat weaker than the oscillations caused by the fundamental cyclotron resonance. The oscillations can be understood as the maximum possible nonresonant scattering in a wave with a rectangular amplitude distribution along the field line.

Since the spread in α_{eq} is too small to be clearly visible in the $\sigma_\varphi(\alpha_{\mathrm{eq}})$ plot from Figure 5i, we re-plot the diffusion with a logarithmic color bar and show the results in Figure 8c. It becomes apparent that we are observing a new type of resonance with a minimum resonant energy near $E_{\mathrm{Rmin}}/2$. This new resonance causes much weaker scattering than the fundamental resonance, but is roughly comparable to nonresonant oscillations. However, when we look at the particle trajectories and diffusion from the simulation with a small-amplitude wave ($B_{\mathrm{w}} = 100\,\mathrm{pT}$), the new resonance becomes much weaker than the nonresonant oscillations, and the corresponding $\sigma_\varphi(\alpha_{\mathrm{eq}})$ values are more than three orders of magnitude below the fundamental resonance effect (Figure 8d–8f).

Based on the numerical observations presented in Figure 8, we identify the new behavior as the nonlinear fractional resonance of order $n = -1/2$. A simplified analytical derivation is provided in Appendix A, where we also identify fractional resonances of order $n = \{\pm 1/3, \pm 1/2, \pm 2/3, \pm 3/2\}$, and suggest that the nonlinear resonance energy spectrum is dense in the sense of rational numbers. These resonances seem to be analogous to the subcyclotron resonance of electrons with whistler waves described within the Hamiltonian framework by Fu et al. (2015). The concept of fractional resonances does not appear in quasilinear theory because it arises from integration along perturbed trajectories (compare with the integration along unperturbed trajectories employed in quasilinear theory as mentioned, e.g., in the theoretical works of Kennel and Engelmann (1966) and Allanson et al. (2022)). In the nonlinear treatment of whistler-electron scattering presented by Omura et al. (2019), an integer resonance is chosen first, and the nonlinear scattering effects are obtained from perturbations of near-resonant electrons. Suppose we instead implement a model of large perturbations without specifying a resonance velocity/energy, as in the example given by Equations (26) and (27), and proceed to analyze power transfer between waves and particles (which is directly related to pitch angle scattering through resonance diffusion curves as explained, e.g., by Summers et al. (1998)). In that case, fractional resonances will arise from the Bessel function expansion of gyrophase evolution. An important property of the $n = -1/2$ is the scaling of scattering strength with the square of wave amplitude – theoretically proven in Equations (44) and (45) – which differs from the known linear dependence for integer resonances. The nonlinear fractional resonances are thus expected to play a role only in precipitation induced by very strong oblique waves.

4 SUMMARY AND DISCUSSION

We have numerically analyzed the dependence of relativistic electron scattering on the wave normal angle and magnetic field amplitude of helium band EMIC waves. Unlike in the previous studies of Wang et al. (2017a) and Lee et al. (2018), we allow for very oblique wave normal angles $\theta_{\mathrm{k}} = 70°$ and $\theta_{\mathrm{k}} = 80°$, and keep the amplitudes more moderate ($B_{\mathrm{w}}/B_{0\mathrm{eq}} < 1\%$). The presented analysis of advective and diffusive behavior is comparable to Bortnik et al. (2022), who, however, used much lower energy and pitch angle resolution and did not include oblique waves. Our results can be divided into three blocks:

1. Confirmation of previous results:
   a. Harmonic resonances $n < -1$ substantially affect the scattering of relativistic electrons at low pitch angles for waves with wave normal angles as small as $\theta_{\mathrm{k}} = 5°$ (Wang et al., 2017a). The contribution from $n > 0$ resonances requires at least moderate obliquity to become significant.
   b. Positive advection of resonant particles at very low pitch angles was detected and shown to dominate over diffusion as wave amplitude increases. This is the effect described as boundary reflection by Zhu et al. (2020) and nonlinear force bunching by Grach and Demekhov (2020) and Bortnik et al. (2022).

c. The advective behavior of resonant particles can be positive or negative, depending on their initial pitch angle and energy (Lee et al., 2018). Particles that start at energies lower than the resonant energy for a given pitch angle will, on average (over gyrophases), experience a decrease in pitch angle, while particles starting at higher energies will encounter the resonance curve at higher latitudes and experience an average increase in pitch angle. This is visualized by the blue-red stripe pairs in Figure 4.

d. Increasing obliquity weakens the effects of $n = -1$ resonance but enhances the resonant interaction for $|n| > 1$ and $n = 1$ (Wang et al., 2017a).

e. Crossings of multiple resonance energies during one passage through the waves result in a more stochastic pitch-angle evolution, described by Lee et al. (2018) as "complicated and time-dependent phase trapping and bunching effects". Under our simplified wave model, these multiresonance effects appear after one quarter-bounce as a fine structure in the plots of advection and diffusion when the EMIC wave is strong and oblique (Figures 4i, 4l, 5i, and 5l).

2. Disagreement with previous results:

a. Oblique waves seem to weaken the advection effects at low pitch angles, contrary to the observations by Lee et al. (2018).

b. We do not observe any effects of precipitation blocking in the PSD analysis (Figure 6), in disagreement with the suggestion presented in Bortnik et al. (2022) that force bunching caused by strong EMIC waves will decrease the electron fluxes/PSD at low pitch angles.

3. New discoveries:

a. Electrons losses of relativistic electrons by quasiparallel waves are comparable to losses induced by oblique waves (Figure 6). This behavior changes for ultrarelativistic electrons ($E_\mathrm{k} \gtrsim 15\,\mathrm{MeV}$, depending on wave parameters), where the very oblique waves cause stronger precipitation.

b. Very oblique waves cannot efficiently scatter electrons at higher pitch angles ($\alpha > 30°$ for $\theta_\mathrm{k} = 80°$, see Figures 5j–5l). Transport from high PSD regions at large pitch angles towards the loss cone is facilitated only by quasiparallel waves.

c. Very oblique waves scatter co-streaming and counter-streaming electrons with similar efficiency due to the high ellipticity, or in other words, due to comparable magnitude of right-handed and left-handed amplitude components (compare Figure 6k with Figure 7i).

d. High-amplitude oblique waves can scatter electrons below minimum resonant energy through nonlinear fractional resonances. The pitch-angle changes caused by $n = -1/2$ scale with the square of wave amplitude, faster than the linear scaling for $n = -1$ resonance.

When comparing our results to previous literature, a few points must be made to avoid confusion: Under our sign convention, the interaction of right-handed waves with electrons happens at resonances of order $n > 1$, and interaction with left-handed waves corresponds with $n < 1$, exactly opposite to the convention used by Wang et al. (2017a). Also, unlike Wang et al. (2017a), we allow only one-quarter bounce, and so $\partial B_0/\partial h > 0$; in the southern hemisphere, the opposite sign of the B_0-field gradient would change the effect of phase trapping on electron pitch angles. Furthermore, the strongest wave we use has a relative amplitude $B_\mathrm{w}/B_0 = 0.64\%$, while Lee et al. (2018) go up to 10% (above the amplitude of the extremely intense EMIC wave observations presented in Engebretson et al. (2015)); as a consequence, phase-trapping has minimal impact on our PSD mapping results, especially for oblique waves.

The disagreement in the dependence of advection on obliquity between our results and Lee et al. (2018) comes from the different approaches to wave modeling. Lee et al. (2018) implements one wave field that is ellipticaly polarized, but remains parallel, and another wave field where the wave normal angle is nonzero, but the polarization remains circular. According to the cold plasma dispersion relation, which is strictly followed in our study, oblique waves always have elliptical polarization (linear being considered as a special case of elliptical), and parallel waves are always circularly polarized, except for the singularity at the crossover frequency. Deviations from circular polarization decrease the advection effects, reconciling our results with Lee et al. (2018).

The lack of precipitation blocking was demonstrated in Section 3.2 through numerical PSD mapping and supported by arguments based on Liouville's theorem. The concept of precipitation blocking was likely first introduced by Grach and Demekhov (2020), who, however, concluded that due to competition between phase trapping and force bunching, the precipitating fluxes would reach the strong diffusion limit, with no apparent decrease near $\alpha = 0^\circ$. Our observations corroborate this conclusion, except that the transport of particles to low pitch angles is due to the symmetric ("diffusive") scattering as observed in Figure 3b, where the particles stay in the phase-trapping region only for a short time and do not become phase-locked. Bortnik et al. (2022) suggested that Van Allen Probes (RBSP) observations of dips in precipitating flux by Zhu et al. (2020) could be explained by force bunching. However, the EMIC-induced precipitating electron flux shown in Zhu et al. (2020) has a local maximum at $\alpha = 0^\circ$, while the force bunching effects should be most effective at removing particles from this region. The spacecraft observations are consistent with the simulation results of Grach and Demekhov (2020), where the PSD distribution sometimes peaked inside the loss cone. This effect is not clearly visible in the perturbed distribution from Figure 6c, because it requires strong phase trapping. Such trapping may be possible with the exceptionally high peak amplitudes $B_\mathrm{w}/B_0 > 1\%$ reported by Zhu et al. (2020), but not with the more moderate values used in our simulations. Recall that transport by phase trapping is nonlocal, allowing mixing of phase space density from distant points along the field line, violating the assumption of a spatially localized electron bunch that we used in our theoretical consideration of PSD evolution (Section 3.2). Finally, we must emphasize that the force bunching does indeed remove particles from the loss cone, but the important quantity for precipitation is the net effect of upward and downward pitch-angle motion.

Most of our new and original results are related to very oblique propagation, which was omitted in previous literature on EMIC-induced precipitation. We have shown that precipitation of relativistic electrons by very oblique waves is comparable to quasiparallel waves, except for electron energies corresponding to high order resonances ($n < -4$). Note that we are not making a comparison to the routinely investigated purely parallel waves with $\theta_\mathrm{k} = 0^\circ$, because in situ spacecraft measurements (Allen et al., 2015) always show at least a small amount of obliquity. Nevertheless, when we consider the increased scattering effects of very oblique waves on counter-streaming electrons, bounce-averaged diffusion might be significantly increased compared to quasiparallel waves. Unfortunately, we do not know how strong the oblique EMIC waves can be, as we are not aware of any study that would show the distribution of wave power over WNA and frequencies. Van Allen Probes observations presented by Saikin et al. (2015) suggest that strong helium-band waves (average wave power $> 0.1\,\mathrm{nT^2/Hz}$) have lower average WNA than weak waves (average wave power from $0.01\,\mathrm{nT^2/Hz}$ to $0.1\,\mathrm{nT^2/Hz}$). Nevertheless, strong waves with $\theta_\mathrm{k} > 60^\circ$ at $L = 5$ were occasionally detected, justifying our parameter choice.

To our knowledge, the nonlinear fractional resonances were never described before in the context of EMIC-electron interaction. They are, however, conceptually identical to the subcyclotron resonance of electrons with whistler waves, which was studied by Fu et al. (2015). (Kramer et al., 2012) detected fractional resonances in fusion devices in the context of ion drift-orbit resonance with magnetohydrodynamic waves. Given the different physical setting, the theoretical approach taken by Kramer et al. (2012) is not the same as ours, but they arrive at a formula consisting of a multi-index sum over a product of Bessel functions, not unlike our Equations (37)–(39). Nonlinear interactions at fractions of the plasma frequency were theoretically described by Lewak and Chen (1969) and used the explain observations made by the Alouette II spacecraft. The EMIC-electron fractional resonances, especially the resonance of order $n = -1/2$, might provide a possible explanation for the precipitation of subrelativistic electrons (Hendry et al. (2017), Hendry et al. (2019), Capannolo et al. (2019), energies in hundreds of keV) if we consider a high-density plasma where the fundamental resonance energy can drop to $1\,\mathrm{MeV}$ (compare with the ω_{pe} dependence plotted in Figure 1). However, to see if this mechanism is competitive with the nonresonant scattering (Chen et al., 2016; An et al., 2022), we need to obtain a realistic distribution of wave power/amplitude over wave normal angles, as mentioned above. Endeavors in this direction are left for future study.

A DERIVATION OF FRACTIONAL RESONANCES

The existence of fractional resonances from Section 3.3 can be derived from the equations of motion for an electron interacting with an elliptically polarized wave. We start by defining the wave field

$$\boldsymbol{E}_{\mathrm{w}} = \hat{\boldsymbol{x}} E_x^{\mathrm{w}} \sin\psi - \hat{\boldsymbol{y}} E_y^{\mathrm{w}} \cos\psi + \hat{\boldsymbol{z}} E_z^{\mathrm{w}} \sin\psi\,, \tag{5}$$

$$\boldsymbol{B}_{\mathrm{w}} = \hat{\boldsymbol{x}} B_x^{\mathrm{w}} \cos\psi + \hat{\boldsymbol{y}} B_y^{\mathrm{w}} \sin\psi - \hat{\boldsymbol{z}} B_z^{\mathrm{w}} \cos\psi\,, \tag{6}$$

where $E_x^{\mathrm{w}} < 0$ and $B_y^{\mathrm{w}} < 0$ for left-hand polarized waves. The three hatted vectors form the standard basis of a Cartesian system. The wave phase seen by a particle with gyrophase φ is

$$\psi = \omega t - k_z z - k_x \rho_{\mathrm{L}} \sin\varphi + \text{const.} \equiv \psi_{\mathrm{B}} - \beta \sin\varphi \tag{7}$$

and includes the effects of finite Larmor radius (FLR) ρ_{L} through the quantity

$$\beta = \frac{\gamma v_\perp k_x}{\Omega_{\mathrm{e}}}\,, \tag{8}$$

while ψ_{B} represents the wave phase at the gyrocenter. The constant initial phase will be dropped in the following analysis.

The equations of motion for an electron with the gyrocenter at $x = y = 0$ propagating through the wave field on a homogeneous background field $\boldsymbol{B_0} \parallel \hat{\boldsymbol{z}}$ (field inhomogeneity is not important for the following resonance spectrum analysis) can be written as

$$\frac{\mathrm{d}(\gamma v_z)}{\mathrm{d}t} = \frac{e}{m}\left(v_\perp B_{\mathrm{R}}^{\mathrm{w}} \sin(\varphi - \psi) + v_\perp B_{\mathrm{L}}^{\mathrm{w}} \sin(\varphi + \psi) - E_z^{\mathrm{w}} \sin\psi\right)\,, \tag{9}$$

$$\frac{\mathrm{d}(\gamma v_\perp)}{\mathrm{d}t} = \frac{e}{m}\left((U_{\mathrm{R}} - v_z) B_{\mathrm{R}}^{\mathrm{w}} \sin(\varphi - \psi) + (U_{\mathrm{L}} - v_z) B_{\mathrm{L}}^{\mathrm{w}} \sin(\varphi + \psi)\right)\,, \tag{10}$$

$$\frac{\mathrm{d}\varphi}{\mathrm{d}t} = \frac{e}{m}\left(\frac{U_{\mathrm{R}} - v_z}{\gamma v_\perp} B_{\mathrm{R}}^{\mathrm{w}} \cos(\varphi - \psi) + \frac{U_{\mathrm{L}} - v_z}{\gamma v_\perp} B_{\mathrm{L}}^{\mathrm{w}} \cos(\varphi + \psi) - \frac{B_z^{\mathrm{w}}}{\gamma} \cos\psi + \frac{B_0}{\gamma}\right)\,. \tag{11}$$

Here we used the decomposition into left- and right-hand polarized components (Omura et al., 2019)

$$\boldsymbol{E}_{\mathbf{R}} = E^{\mathrm{w}}_{\mathrm{R}} \left(\hat{\boldsymbol{x}} \sin\psi - \hat{\boldsymbol{y}} \cos\psi \right) \,, \quad E^{\mathrm{w}}_{\mathrm{R}} = \frac{E^{\mathrm{w}}_x + E^{\mathrm{w}}_y}{2} \,, \tag{12}$$

$$\boldsymbol{E}_{\mathbf{L}} = E^{\mathrm{w}}_{\mathrm{L}} \left(-\hat{\boldsymbol{x}} \sin\psi - \hat{\boldsymbol{y}} \cos\psi \right) \,, \quad E^{\mathrm{w}}_{\mathrm{L}} = \frac{E^{\mathrm{w}}_y - E^{\mathrm{w}}_y}{2} \,, \tag{13}$$

$$\boldsymbol{B}_{\mathbf{R}} = B^{\mathrm{w}}_{\mathrm{R}} \left(\hat{\boldsymbol{x}} \cos\psi + \hat{\boldsymbol{y}} \sin\psi \right) \,, \quad B^{\mathrm{w}}_{\mathrm{R}} = \frac{B^{\mathrm{w}}_x + B^{\mathrm{w}}_y}{2} \,, \tag{14}$$

$$\boldsymbol{B}_{\mathbf{L}} = B^{\mathrm{w}}_{\mathrm{L}} \left(\hat{\boldsymbol{x}} \cos\psi - \hat{\boldsymbol{y}} \sin\psi \right) \,, \quad B^{\mathrm{w}}_{\mathrm{L}} = \frac{B^{\mathrm{w}}_x - B^{\mathrm{w}}_y}{2} \tag{15}$$

$$\tag{16}$$

and defined the ratios

$$U_{\mathrm{R}} = \frac{E^{\mathrm{w}}_{\mathrm{R}}}{B^{\mathrm{w}}_{\mathrm{R}}} \,, \quad U_{\mathrm{L}} = \frac{E^{\mathrm{w}}_{\mathrm{L}}}{B^{\mathrm{w}}_{\mathrm{L}}} \,, \tag{17}$$

which are related to phase velocities (they reduce exactly to phase velocities in case of circularly polarized parallel-propagating waves). In further calculations, we will also use the normalized amplitude components $\Omega^{\mathrm{w}}_{\mathrm{R}} = B^{\mathrm{w}}_{\mathrm{R}} e/m$, $\Omega^{\mathrm{w}}_{\mathrm{L}} = B^{\mathrm{w}}_{\mathrm{L}} e/m$ and $\Omega^{\mathrm{w}}_z = B^{\mathrm{w}}_z e/m$.

The average change in electron kinetic energy per one wave period T can be expressed as

$$\begin{aligned} \left\langle \frac{\mathrm{d}E_{\mathrm{k}}}{\mathrm{d}t} \right\rangle_T &= -\frac{e}{T} \int_0^T \mathrm{d}t (\boldsymbol{v} \cdot \boldsymbol{E}_{\mathbf{w}}) = \\ &= -\frac{e}{T} \int_0^T \mathrm{d}t \left(v_\perp (E^{\mathrm{w}}_{\mathrm{R}} - E^{\mathrm{w}}_{\mathrm{L}}) \cos\varphi \sin\psi - v_\perp (E^{\mathrm{w}}_{\mathrm{R}} + E^{\mathrm{w}}_{\mathrm{L}}) \sin\varphi \cos\psi + v_z E^{\mathrm{w}}_{\mathrm{z}} \sin\psi \right) \,, \end{aligned} \tag{18}$$

where we used the decompositions from Equations (12)–(15). Let us denote the integrand I and restate it in the form

$$I = -\frac{e}{T} \left(-v_\perp \left(E^{\mathrm{w}}_{\mathrm{R}} \sin(\varphi - \psi) + E^{\mathrm{w}}_{\mathrm{L}} \sin(\varphi + \psi) \right) + v_z E^{\mathrm{w}}_z \sin\psi \right) \,. \tag{19}$$

We may now apply the Jacobi-Anger expansion (Abramowitz and Stegun, 1965) and express the trigonometric functions in terms of Bessel functions of the first kind,

$$\sin(\varphi - \psi) = \sin(\varphi - \psi_{\mathrm{B}} + \beta \sin\varphi) = \sum_{n=-\infty}^{\infty} J_{n-1}(\beta) \sin\zeta_n = \sum_{n=-\infty}^{\infty} J_n(\beta) \sin\zeta_{n+1} \,, \tag{20}$$

$$\sin(\varphi + \psi) = \sin(\varphi + \psi_{\mathrm{B}} - \beta \sin\varphi) = -\sum_{n=-\infty}^{\infty} J_{n+1}(\beta) \sin\zeta_n = -\sum_{n=-\infty}^{\infty} J_n(\beta) \sin\zeta_{n-1} \,, \tag{21}$$

$$\sin(\psi) = \sin(\psi_{\mathrm{B}} - \beta \sin\varphi) = -\sum_{n=-\infty}^{\infty} J_n(\beta) \sin\zeta_n \,, \tag{22}$$

$$\tag{23}$$

where

$$\zeta_n = n\varphi - \psi_B \tag{24}$$

is the relative phase angle for the n-th resonance. Note that while the changes in kinetic energy of electrons interacting with EMIC waves are typically negligible, these small energy changes are directly related to large changes in pitch angle through the particle motion along resonant diffusion curves (Summers et al., 1998).

The nonlinear effect of individual resonances is usually studied by performing an expansion in v_z about the n-th resonance velocity

$$V_{\mathrm{R}n} = \frac{1}{k_z}\left(\omega + \frac{n\Omega_{\mathrm{e}}}{\gamma}\right) . \tag{25}$$

Here we instead expand the gyrophase to the first order of perturbations due to wave-particle interactions, and plug them into the Jacobi-Anger expansions from Equations (20)–(22). Let us write $\varphi \approx \varphi_0 + \varphi_1$ with

$$\frac{\mathrm{d}\varphi_0}{\mathrm{d}t} = \frac{\Omega_{\mathrm{e}}}{\gamma} , \tag{26}$$

$$\frac{\mathrm{d}\varphi_1}{\mathrm{d}t} = -\frac{v_z}{\gamma v_\perp}\Omega_{\mathrm{R}}^{\mathrm{w}}\cos(\varphi - \psi) - \frac{v_z}{\gamma v_\perp}\Omega_{\mathrm{R}}^{\mathrm{w}}\cos(\varphi + \psi) , \tag{27}$$

where we have used the inequalities $|U_{\mathrm{L}}| \ll |v_z|$ and $|U_{\mathrm{R}}| \ll |v_z|$ for EMIC waves and relativistic electrons, and we also removed the Ω_z^{w} term by focusing on low pitch angle regions where $\Omega_z^{\mathrm{w}} \ll \Omega_{\mathrm{R,L}}^{\mathrm{w}} v_z/\gamma v_\perp$. For simplicity, we will further neglect the perturbations to v_z and $v_\perp$. In the case of $v_\perp$, the factors in front of sines in Equation (10), divided by $\gamma v_\perp$, are the same as the factors in front of cosines in Equation (11), suggesting that the relative perturbations in $v_\perp$ and φ are comparable. However, $v_\perp$ enters the computation either through $\mathrm{d}\varphi_1/\mathrm{d}t$, so we can consider that perturbation to be of second order, or through β, which simply scales the FLR effects and can be thus kept constant without losing information about resonant behavior. In the case of v_z, the approximation can be justified only for low pitch angles since comparing the factors in Equations (9) and (11) sets the requirement $v_\perp/v_z \ll v_z/v_\perp$ (v_z enters directly into ψ through $k_z z = k_z v_z t$, so the perturbation would be of the first order if we did not use the low α approximation).

The cut off the perturbation expansion, we replace ψ by ψ_{B} in Equations (26) and (27). The perturbation φ_1 can then be obtained by integrating over time,

$$\varphi_1 = -R_1\sin(\varphi_0 - \psi_{\mathrm{B}}) - L_1\sin(\varphi_0 + \psi_{\mathrm{B}}) . \tag{28}$$

Here we introduced the substitutions

$$R_1 = \frac{v_z}{v_\perp}\frac{\Omega_{\mathrm{R}}}{\nu_1} , \tag{29}$$

$$L_1 = \frac{v_z}{v_\perp}\frac{\Omega_{\mathrm{L}}}{\nu_{-1}} , \tag{30}$$

where

$$\nu_{\pm 1} = \Omega_{\mathrm{e}} \mp \omega \pm k_z v_z \tag{31}$$

is a quantity expressing the deviation from the fundamental resonances $n = \pm 1$.

475 Going back to the Bessel function expansion from Equations (20)–(22), we can now write

$$\sin\zeta_n \approx \sin\left(n(\varphi_0+\varphi_1)-\psi_\mathrm{B}\right) = \sin\left(n\varphi_0 - nR_1\sin(\varphi_0-\psi_\mathrm{B})\right)\cos\left(-\psi_\mathrm{B}-nL_1\sin(\varphi_0+\psi_\mathrm{B})\right)+ \\ + \cos\left(n\varphi_0 - nR_1\sin(\varphi_0-\psi_\mathrm{B})\right)\sin\left(-\psi_\mathrm{B}-nL_1\sin(\varphi_0+\psi_\mathrm{B})\right)\ . \tag{32}$$

Using the second form of the expansions, we can expand each of the trigonometric functions from Equation (32) into

$$\sin\left(n\varphi_0 - nR_1\sin(\varphi_0-\psi_\mathrm{B})\right) = -\sum_{r=-\infty}^{\infty} J_r(nR_1)\sin\left(r(\varphi_0-\psi_\mathrm{B})-n\varphi_0\right)\ , \tag{33}$$

$$\cos\left(-\psi_\mathrm{B}-nL_1\sin(\varphi_0+\psi_\mathrm{B})\right) = \sum_{l=-\infty}^{\infty} J_l(nL_1)\cos\left(l(\varphi_0+\psi_\mathrm{B})+\psi_\mathrm{B}\right)\ , \tag{34}$$

$$\cos\left(n\varphi_0 - nR_1\sin(\varphi_0-\psi_\mathrm{B})\right) = \sum_{r=-\infty}^{\infty} J_r(nR_1)\cos\left(r(\varphi_0-\psi_\mathrm{B})-n\varphi_0\right)\ , \tag{35}$$

$$\sin\left(-\psi_\mathrm{B}-nL_1\sin(\varphi_0+\psi_\mathrm{B})\right) = -\sum_{l=-\infty}^{\infty} J_l(nL_1)\sin\left(l(\varphi_0+\psi_\mathrm{B})+\psi_\mathrm{B}\right)\ . \tag{36}$$

Since R_1 and L_1 are proportional to the relative wave magnetic field B_w/B_0, we can limit the summations to $|r|\leq 1$ and $|l|\leq 1$. As a further simplification, we will limit the resonance number n to $-1, 0, 1$, which is a reasonable approximation when $\beta^2 \ll 1$, i. e., when pitch angles are low and θ_k is not too close to the resonance cone. We then insert the Equations (33)–(36) into Equations (32) and (20)–(22) and finally obtain

$$\sin(\varphi-\psi) \approx -\sum_{n,r,l=-1}^{1} J_n(\beta)J_r((n+1)R_1)J_l((n+1)L_1)\sin\left((r-n+l-1)\varphi_0+(l-r+1)\psi_B\right)\ , \tag{37}$$

$$\sin(\varphi+\psi) \approx \sum_{n,r,l=-1}^{1} J_n(\beta)J_r((n-1)R_1)J_l((n-1)L_1)\sin\left((r-n+l+1)\varphi_0+(l-r+1)\psi_B\right)\ , \tag{38}$$

$$\sin(\psi) \approx -\sum_{n,r,l=-1}^{1} J_n(\beta)J_r(nR_1)J_l(nL_1)\sin\left((r-n+l)\varphi_0+(l-r+1)\psi_B\right)\ . \tag{39}$$

Comparing the prefactors of φ_0 and ψ results in resonant fractions

$$q_\mathrm{R} = -\frac{r-n+l-1}{l-r+1}\ , \tag{40}$$

$$q_\mathrm{L} = -\frac{r-n+l+1}{l-r+1}\ , \tag{41}$$

$$q_\mathrm{z} = -\frac{r-n+l}{l-r+1}\ . \tag{42}$$

Apart from the integer values (which represent fundamental and harmonic resonances), the fractions can also evaluate to $\pm 1/3$, $\pm 1/2$, $\pm 2/3$, and $\pm 3/2$; other fractional values would appear if we extended the summation range in n and removed the approximation $\beta^2 \ll 1$.

Let us focus on the resonance $-1/2$ which contributes to electron diffusion near $E_\mathrm{k} = 2\,\mathrm{MeV}$ in Figure 8c. The related relative phase angle $\varphi_0 + 2\psi_\mathrm{B}$ corresponds to resonance velocity

$$V_{\mathrm{R}-1/2} = \frac{1}{k_z}\left(\omega - \frac{\Omega_\mathrm{e}}{2\gamma}\right) . \tag{43}$$

Going back to the average change in energy defined in Equation (18), we can perform the Taylor expansion of Bessel function to the first order and show that term with E_R^w does not contribute to the $-1/2$ resonance, while the E_L^w contributes to the integrand by

$$-\frac{e\gamma k_x v_\perp v_z E_\mathrm{L}^\mathrm{w} \Omega_\mathrm{R}^\mathrm{w}}{2T\Omega_\mathrm{e}\nu_1} , \tag{44}$$

where we have used Equations (29) and (8). The E_z^w also has a nonzero contribution to the integrand,

$$-\frac{e v_z^2 E_z^\mathrm{w} \Omega_\mathrm{L}^\mathrm{w}}{2T v_\perp \nu_{-1}} . \tag{45}$$

Due to the terms $E_\mathrm{L}^\mathrm{w}\Omega_\mathrm{R}^\mathrm{w}$ and $E_z^\mathrm{w}\Omega_\mathrm{L}^\mathrm{w}$, the energy change caused by $-1/2$ resonance scales with a square of the wave amplitude. On the other hand, for the integer resonance terms with $r = l = 0$, the quantities $\Omega_\mathrm{R}^\mathrm{w}$ and $\Omega_\mathrm{L}^\mathrm{w}$ disappear, and the scaling reduces to the first power in amplitude. This analytical result explains the diminishing of the $-1/2$ resonance in Figure 8 when the amplitude is decreased. Notice that due to the term $1/\nu_{-1}$, fractional resonances very close to $n = -1$ retain non-negligible strength and contribute to resonance broadening.

The derivation provided in this section works for whistler-mode waves as well, except for the approximations $U_\mathrm{R} \ll v_z$, $U_\mathrm{L} \ll v_z$.

CONFLICT OF INTEREST STATEMENT

The authors declare that the research was conducted in the absence of any commercial or financial relationships that could be construed as a potential conflict of interest.

AUTHOR CONTRIBUTIONS

TODO-complete-before-submission. MH wrote and ran the simulation code, analyzed the resulting data, derived the equations for fractional resonances, and prepared the original draft. WL initiated the study and provided frequent consultations. QM helped in validating the code. WL and QM provided advice during the pre-submission review and editing of the manuscript.

FUNDING

TODO [Details of all funding sources should be provided, including grant numbers if applicable. Please ensure to add all necessary funding information, as after publication this is no longer possible.]

ACKNOWLEDGMENTS

TODO Murong and Xiaochen for joining the discussions? Jacob Bortnik and Xin An for commenting on precipitation blocking? [This is a short text to acknowledge the contributions of specific colleagues, institutions, or agencies that aided the efforts of the authors.]

DATA AVAILABILITY STATEMENT

TODO The dataset is huge because of the high-resolution particle trajectories. Is it ok to provide only the code and instructions? Or can I keep only the trajectories that appear in Figure 3? [The datasets [GENERATED/ANALYZED] for this study can be found in the [NAME OF REPOSITORY] [LINK].]

REFERENCES

Abramowitz, M. and Stegun, I. A. (1965). *Handbook of Mathematical Functions: With Formulas, Graphs, and Mathematical Tables*. Dover Books on Advanced Mathematics (Dover Publications, New York)

Allanson, O., Elsden, T., Watt, C., and Neukirch, T. (2022). Weak turbulence and quasilinear diffusion for relativistic wave-particle interactions via a Markov approach. *Front. Astron. Space Sci.* 8, 232. doi:10.3389/fspas.2021.805699

Allen, R. C., Zhang, J. C., Kistler, L. M., Spence, H. E., Lin, R. L., Klecker, B., et al. (2015). A statistical study of EMIC waves observed by Cluster: 1. Wave properties. *J. Geophys. Res. Space Physics* 120, 5574–5592. doi:10.1002/2015JA021333

An, X., Artemyev, A., Angelopoulos, V., Zhang, X., Mourenas, D., and Bortnik, J. (2022). Nonresonant Scattering of Relativistic Electrons by Electromagnetic Ion Cyclotron Waves in Earth's Radiation Belts. *Phys. Rev. Lett.* 129, 135101. doi:10.1103/PhysRevLett.129.135101

Anderson, B. J., Denton, R. E., Ho, G., Hamilton, D. C., Fuselier, S. A., and Strangeway, R. J. (1996). Observational test of local proton cyclotron instability in the Earth's magnetosphere. *J. Geophys. Res.* 101, 21527–21544. doi:10.1029/96JA01251

Artemyev, A. V., Neishtadt, A. I., Vainchtein, D. L., Vasiliev, A. A., Vasko, I. Y., and Zelenyi, L. M. (2018). Trapping (capture) into resonance and scattering on resonance: Summary of results for space plasma systems. *Commun. Nonlinear Sci. Numer. Simulat.* 65, 111–160. doi:10.1016/j.cnsns.2018.05.004

Bortnik, J., Albert, J. M., Artemyev, A., Li, W., Jun, C.-W., Grach, V. S., et al. (2022). Amplitude Dependence of Nonlinear Precipitation Blocking of Relativistic Electrons by Large Amplitude EMIC Waves. *Geophys. Res. Lett.* 49, e98365. doi:10.1029/2022GL098365

Capannolo, L., Li, W., Ma, Q., Chen, L., Shen, X. C., Spence, H. E., et al. (2019). Direct Observation of Subrelativistic Electron Precipitation Potentially Driven by EMIC Waves. *Geophys. Res. Lett.* 46, 12,711–12,721. doi:10.1029/2019GL084202

Chen, L., Thorne, R. M., Bortnik, J., and Zhang, X.-J. (2016). Nonresonant interactions of electromagnetic ion cyclotron waves with relativistic electrons. *J. Geophys. Res. Space Physics* 121, 9913–9925. doi:10.1002/2016JA022813

Clilverd, M. A., Duthie, R., Hardman, R., Hendry, A. T., Rodger, C. J., Raita, T., et al. (2015). Electron precipitation from EMIC waves: A case study from 31 May 2013. *J. Geophys. Res. Space Physics* 120, 3618–3631. doi:10.1002/2015JA021090

Denton, R. E., Goldstein, J., Menietti, J. D., and Young, S. L. (2002). Magnetospheric electron density model inferred from Polar plasma wave data. *J. Geophys. Res. Space Physics* 107, 1386. doi:10.1029/2001JA009136

Engebretson, M. J., Posch, J. L., Wygant, J. R., Kletzing, C. A., Lessard, M. R., Huang, C. L., et al. (2015). Van Allen probes, NOAA, GOES, and ground observations of an intense EMIC wave event extending over 12 h in magnetic local time. *J. Geophys. Res. Space Physics* 120, 5465–5488. doi:10.1002/2015JA021227

Fu, X., Guo, Z., Dong, C., and Gary, S. P. (2015). Nonlinear subcyclotron resonance as a formationmechanism for gaps in banded chorus. *Geophys. Res. Lett.* 42, 3150–3159. doi:10.1002/2015GL064182

Grach, V. S., Artemyev, A. V., Demekhov, A. G., Zhang, X.-J., Bortnik, J., Angelopoulos, V., et al. (2022). Relativistic Electron Precipitation by EMIC Waves: Importance of Nonlinear Resonant Effects. *Geophys. Res. Lett.* 49, e99994. doi:10.1029/2022GL099994

Grach, V. S. and Demekhov, A. G. (2020). Precipitation of Relativistic Electrons Under Resonant Interaction With Electromagnetic Ion Cyclotron Wave Packets. *J. Geophys. Res. Space Physics* 125, e27358. doi:10.1029/2019JA027358

Hanzelka, M., Santolík, O., Omura, Y., and Kolmašová, I. (2021). Measurability of the Nonlinear Response of Electron Distribution Function to Chorus Emissions in the Earth's Radiation Belt. *J. Geophys. Res. Space Physics* 126, e29624. doi:10.1029/2021JA029624

Hendry, A. T., Rodger, C. J., and Clilverd, M. A. (2017). Evidence of sub-MeV EMIC-driven electron precipitation. *Geophys. Res. Lett.* 44, 1210–1218. doi:10.1002/2016GL071807

Hendry, A. T., Santolik, O., Kletzing, C. A., Rodger, C. J., Shiokawa, K., and Baishev, D. (2019). Multi-instrument Observation of Nonlinear EMIC-Driven Electron Precipitation at sub-MeV Energies. *Geophys. Res. Lett.* 46, 7248–7257. doi:10.1029/2019GL082401

Horne, R. B. and Thorne, R. M. (1998). Potential waves for relativistic electron scattering and stochastic acceleration during magnetic storms. *Geophys. Res. Lett.* 25, 3011–3014. doi:10.1029/98GL01002

Horwitz, J. L., Baugher, C. R., Chappell, C. R., Shelley, E. G., Young, D. T., and Anderson, R. R. (1981). ISEE 1 observations of thermal plasma in the vicinity of the plasmasphere during periods of quieting magnetic activity. *J. Geophys. Res.* 86, 9989–10001. doi:10.1029/JA086iA12p09989

Ichimaru, S. (2004). *Statistical Plasma Physics: Basic Principles (1st ed.)* (CRC Press)

Jordanova, V. K., Albert, J., and Miyoshi, Y. (2008). Relativistic electron precipitation by EMIC waves from self-consistent global simulations. *J. Geophys. Res. Space Physics* 113, A00A10. doi:10.1029/2008JA013239

Jun, C.-W., Miyoshi, Y., Kurita, S., Yue, C., Bortnik, J., Lyons, L., et al. (2021). The Characteristics of EMIC Waves in the Magnetosphere Based on the Van Allen Probes and Arase Observations. *J. Geophys. Res. Space Physics* 126, e29001. doi:10.1029/2020JA029001

Karpman, V. I. (1974). Nonlinear Effects in the ELF Waves Propagating along the Magnetic Field in the Magnetosphere. *Space Sci. Rev.* 16, 361–388. doi:10.1007/BF00171564

Kennel, C. F. and Engelmann, F. (1966). Velocity Space Diffusion from Weak Plasma Turbulence in a Magnetic Field. *Phys. Fluids* 9, 2377–2388. doi:10.1063/1.1761629

Kennel, C. F. and Petschek, H. E. (1966). Limit on Stably Trapped Particle Fluxes. *J. Geophys. Res.* 71, 1–28. doi:10.1029/JZ071i001p00001

Kim, E.-H. and Johnson, J. R. (2016). Full-wave modeling of EMIC waves near the He^+ gyrofrequency. *Geophys. Res. Lett.* 43, 13–21. doi:10.1002/2015GL066978

Kramer, G. J., Chen, L., Fisher, R. K., Heidbrink, W. W., Nazikian, R., Pace, D. C., et al. (2012). Fractional Resonances between Waves and Energetic Particles in Tokamak Plasmas. *Phys. Rev. Lett.* 109, 035003. doi:10.1103/PhysRevLett.109.035003

Kurita, S., Miyoshi, Y., Shiokawa, K., Higashio, N., Mitani, T., Takashima, T., et al. (2018). Rapid Loss of Relativistic Electrons by EMIC Waves in the Outer Radiation Belt Observed by Arase, Van Allen Probes, and the PWING Ground Stations. *Geophys. Res. Lett.* 45, 12,720–12,729. doi:10.1029/2018GL080262

Lee, D.-Y., Shin, D.-K., and Choi, C.-R. (2018). Effects of Oblique Wave Normal Angle and Noncircular Polarization of Electromagnetic Ion Cyclotron Waves on the Pitch Angle Scattering of Relativistic Electrons. *J. Geophys. Res. Space Physics* 123, 4556–4573. doi:10.1029/2018JA025342

Lewak, G. J. and Chen, C. S. (1969). Higher order resonances in a plasma. *J. Plasma Phys.* 3, 481–497. doi:10.1017/S0022377800004554

Li, W. and Hudson, M. K. (2019). Earth's Van Allen Radiation Belts: From Discovery to the Van Allen Probes Era. *J. Geophys. Res. Space Physics* 124, 8319–8351. doi:10.1029/2018JA025940

Loto'aniu, T. M., Fraser, B. J., and Waters, C. L. (2005). Propagation of electromagnetic ion cyclotron wave energy in the magnetosphere. *J. Geophys. Res. Space Physics* 110, A07214. doi:10.1029/2004JA010816

Meredith, N. P., Horne, R. B., Kersten, T., Fraser, B. J., and Grew, R. S. (2014). Global morphology and spectral properties of EMIC waves derived from CRRES observations. *J. Geophys. Res. Space Physics* 119, 5328–5342. doi:10.1002/2014JA020064

Meredith, N. P., Thorne, R. M., Horne, R. B., Summers, D., Fraser, B. J., and Anderson, R. R. (2003). Statistical analysis of relativistic electron energies for cyclotron resonance with EMIC waves observed on CRRES. *J. Geophys. Res. Space Physics* 108, 1250. doi:10.1029/2002JA009700

Min, K., Lee, J., Keika, K., and Li, W. (2012). Global distribution of EMIC waves derived from THEMIS observations. *J. Geophys. Res. Space Physics* 117, A05219. doi:10.1029/2012JA017515

Nunn, D. and Omura, Y. (2015). A computational and theoretical investigation of nonlinear wave-particle interactions in oblique whistlers. *J. Geophys. Res. Space Physics* 120, 2890–2911. doi:10.1002/2014JA020898

Omura, Y. (2021). Nonlinear wave growth theory of whistler-mode chorus and hiss emissions in the magnetosphere. *Earth Planets Space* 73, 95. doi:10.1186/s40623-021-01380-w

Omura, Y., Hsieh, Y.-K., Foster, J. C., Erickson, P. J., Kletzing, C. A., and Baker, D. N. (2019). Cyclotron Acceleration of Relativistic Electrons Through Landau Resonance With Obliquely Propagating Whistler-Mode Chorus Emissions. *J. Geophys. Res. Space Physics* 124, 2795–2810. doi:10.1029/2018JA026374

Omura, Y., Pickett, J., Grison, B., Santolik, O., Dandouras, I., Engebretson, M., et al. (2010). Theory and observation of electromagnetic ion cyclotron triggered emissions in the magnetosphere. *J. Geophys. Res. Space Physics* 115, A07234. doi:10.1029/2010JA015300

Omura, Y. and Zhao, Q. (2012). Nonlinear pitch angle scattering of relativistic electrons by EMIC waves in the inner magnetosphere. *J. Geophys. Res. Space Physics* 117, A08227. doi:10.1029/2012JA017943

Perraut, S., Gendrin, R., Roux, A., and de Villedary, C. (1984). Ion cyclotron waves: Direct comparison between ground-based measurements and observations in the source region. *J. Geophys. Res.* 89, 195–202. doi:10.1029/JA089iA01p00195

Rauch, J. L. and Roux, A. (1982). Ray tracing of ULF waves in a multicomponent magnetospheric plasma: Consequences for the generation mechanism of ion cyclotron waves. *J. Geophys. Res.* 87, 8191–8198. doi:10.1029/JA087iA10p08191

Saikin, A. A., Zhang, J. C., Allen, R. C., Smith, C. W., Kistler, L. M., Spence, H. E., et al. (2015). The occurrence and wave properties of H^+-, He^+-, and O^+-band EMIC waves observed by the Van Allen Probes. *J. Geophys. Res. Space Physics* 120, 7477–7492. doi:10.1002/2015JA021358

Saito, T. (1969). Geomagnetic Pulsations. *Space Sci. Rev.* 10, 319–412. doi:10.1007/BF00203620

Shoji, M., Miyoshi, Y., Kistler, L. M., Asamura, K., Matsuoka, A., Kasaba, Y., et al. (2021). Discovery of proton hill in the phase space during interactions between ions and electromagnetic ion cyclotron waves. *Sci. Rep.* 11, 13480. doi:10.1038/s41598-021-92541-0

Stix, T. (1992). *Waves in Plasmas* (Melville NY: American Institute of Physics)

Summers, D., Omura, Y., Miyashita, Y., and Lee, D.-H. (2012). Nonlinear spatiotemporal evolution of whistler mode chorus waves in Earth's inner magnetosphere. *J. Geophys. Res. Space Physics* 117, A09206. doi:10.1029/2012JA017842

Summers, D., Thorne, R. M., and Xiao, F. (1998). Relativistic theory of wave-particle resonant diffusion with application to electron acceleration in the magnetosphere. *J. Geophys. Res.* 103, 20487–20500. doi:10.1029/98JA01740

Thorne, R. M. and Kennel, C. F. (1971). Relativistic electron precipitation during magnetic storm main phase. *J. Geophys. Res.* 76, 4446. doi:10.1029/JA076i019p04446

Usanova, M. E., Drozdov, A., Orlova, K., Mann, I. R., Shprits, Y., Robertson, M. T., et al. (2014). Effect of EMIC waves on relativistic and ultrarelativistic electron populations: Ground-based and Van Allen Probes observations. *Geophys. Res. Lett.* 41, 1375–1381. doi:10.1002/2013GL059024

Usanova, M. E., Mann, I. R., Bortnik, J., Shao, L., and Angelopoulos, V. (2012). THEMIS observations of electromagnetic ion cyclotron wave occurrence: Dependence on AE, SYMH, and solar wind dynamic pressure. *J. Geophys. Res. Space Physics* 117, A10218. doi:10.1029/2012JA018049

Wang, G., Su, Z., Zheng, H., Wang, Y., Zhang, M., and Wang, S. (2017a). Nonlinear fundamental and harmonic cyclotron resonant scattering of radiation belt ultrarelativistic electrons by oblique monochromatic EMIC waves. *J. Geophys. Res. Space Physics* 122, 1928–1945. doi:10.1002/2016JA023451

Wang, X. Y., Huang, S. Y., Allen, R. C., Fu, H. S., Deng, X. H., Zhou, M., et al. (2017b). The occurrence and wave properties of EMIC waves observed by the Magnetospheric Multiscale (MMS) mission. *J. Geophys. Res. Space Physics* 122, 8228–8240. doi:10.1002/2017JA024237

Xiao, F., Thorne, R. M., and Summers, D. (1998). Instability of electromagnetic R-mode waves in a relativistic plasma. *Phys. Plasmas* 5, 2489–2497. doi:10.1063/1.872932

Zenitani, S. and Umeda, T. (2018). On the Boris solver in particle-in-cell simulation. *Phys. Plasmas* 25, 112110. doi:10.1063/1.5051077

Zhao, H., Johnston, W. R., Baker, D. N., Li, X., Ni, B., Jaynes, A. N., et al. (2019). Characterization and Evolution of Radiation Belt Electron Energy Spectra Based on the Van Allen Probes Measurements. *J. Geophys. Res. Space Physics* 124, 4217–4232. doi:10.1029/2019JA026697

Zheng, L., Chen, L., and Zhu, H. (2019). Modeling Energetic Electron Nonlinear Wave-Particle Interactions With Electromagnetic Ion Cyclotron Waves. *J. Geophys. Res. Space Physics* 124, 3436–3453. doi:10.1029/2018JA026156

Zhu, H., Chen, L., Claudepierre, S. G., and Zheng, L. (2020). Direct Evidence of the Pitch Angle Scattering of Relativistic Electrons Induced by EMIC Waves. *Geophys. Res. Lett.* 47, e85637. doi:10.1029/2019GL085637

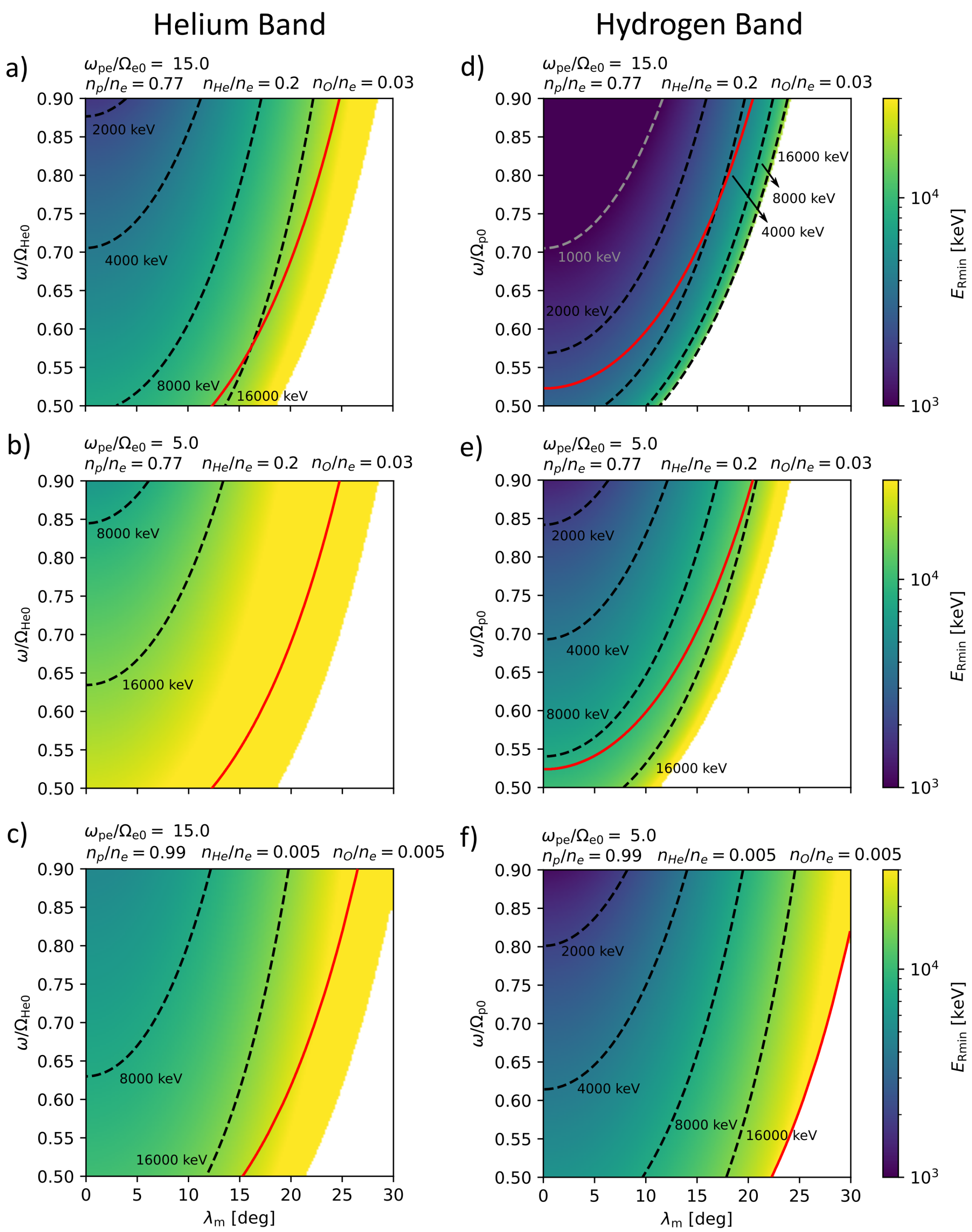

Figure 1. Minimum resonant energies E_{Rmin} of electrons interacting with a left-hand polarized parallel propagating EMIC wave. Each panel shows a map of energies in dependence on wave frequency and magnetic latitude. (a) Minimum resonant energies for interaction with a helium-band wave in a high-density plasma with a high relative concentration of heavier ions – these conditions are used in our simulations. (b) Same as panel a, but in a low-density plasma. (c) Same as panel (a), but with a low concentration of heavier ions. Panels (d)–(f) show E_{Rmin} for a hydrogen band wave under the same plasma conditions as in panels (a)–(c), except for panel f, where both the electron density and heavier ion concentrations are kept low. In all panels, dashed lines represent energy contours, and the solid red line signifies the crossover frequency. Note that for oblique waves, the left-handed dispersion branch is coupled to the right-handed branch, so the energies right of the red curve would have to be calculated for right-hand polarized waves.

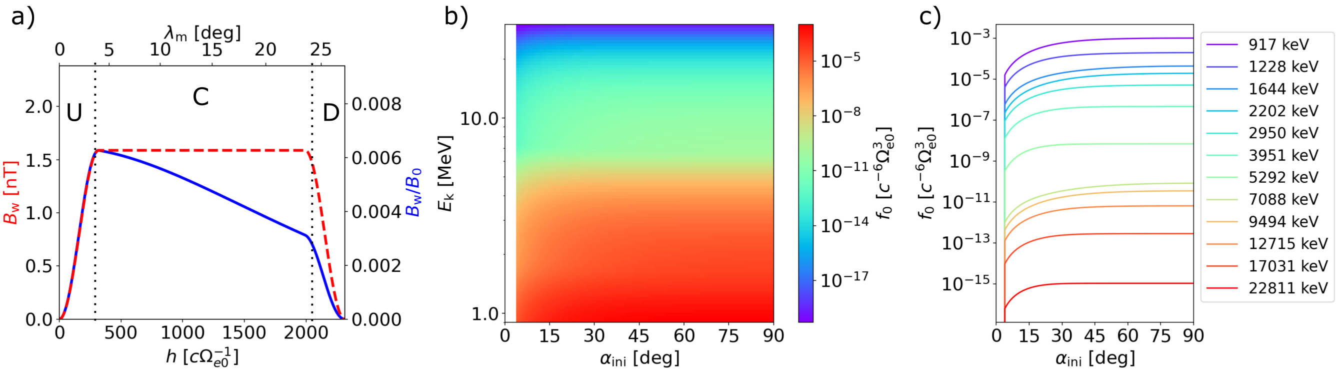

Figure 2. (a) Distribution of wave amplitudes along the field line. The wave experiences smooth growth in region U, stays constant in region C ($1.6\,\mathrm{nT}$ in this example), and decreases back to zero in region D, as shown by the dashed red line. The solid blue line shows the relative wave amplitude with respect to the background field B_0. (b) Phase space density distribution at the equator plotted in the energy–pitch angle space. The empty loss cone corresponds to the white region at $\alpha_{\mathrm{ini}} < \alpha_{\mathrm{loss}} = 3.7°$. Normalized PSD units from the simulation code are used. (c) Line plots of pitch angle profiles from the previous panel for representative energies. Note that the $\sin\alpha$ term from Jacobian is not included; therefore, the decrease in PSD near loss cone indicates positive pitch-angle anisotropy.

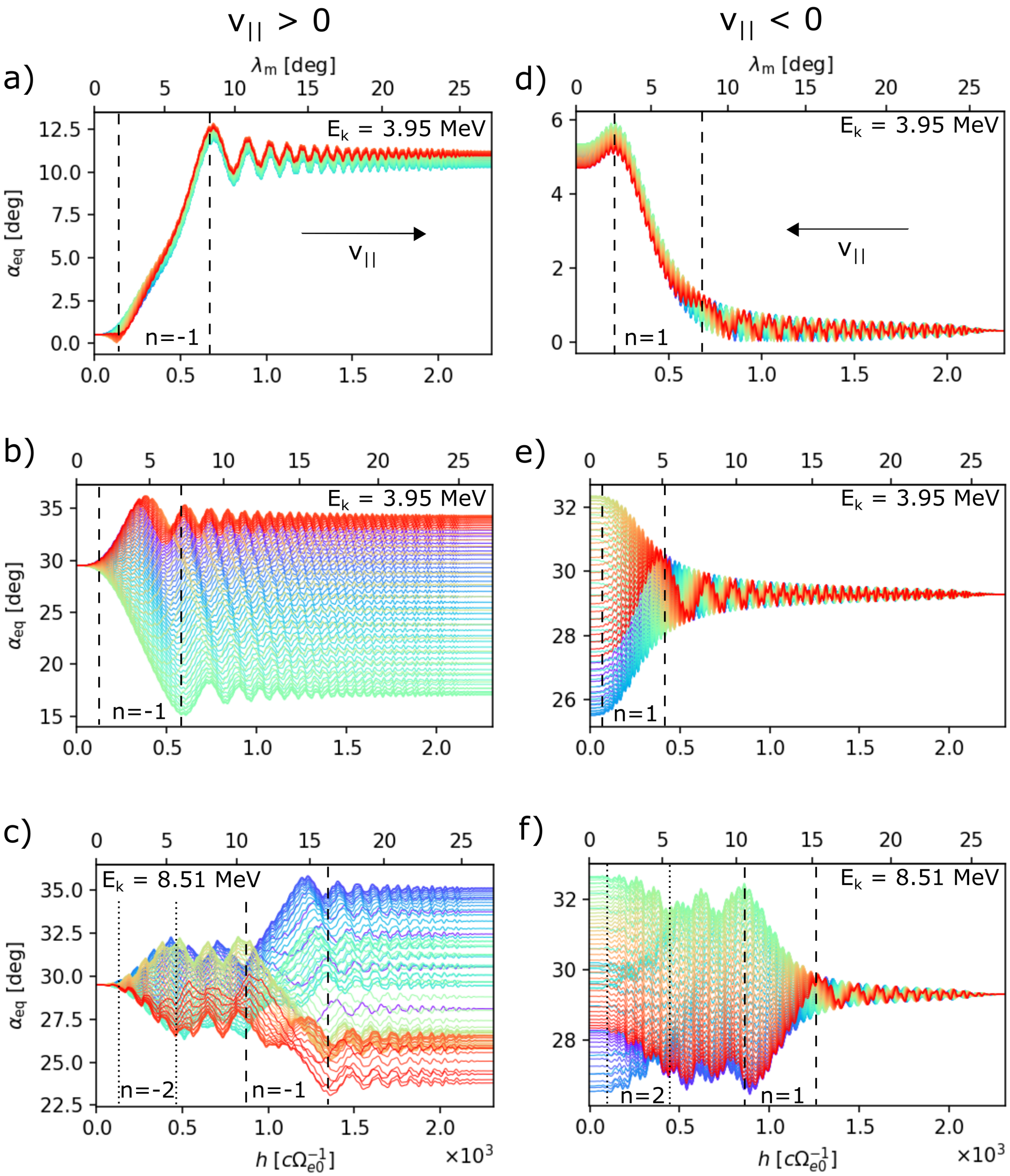

Figure 3. Trajectory examples showing the change in equatorial pitch angle over latitude due to interaction with a high-amplitude, moderately oblique wave ($B_\mathrm{w}/B_{0\mathrm{eq}} = 0.0064$ and $\theta_\mathrm{k} = 45°$). Panels (a)–(c) depict electrons propagating along the wave (from the equator), while panels (d)–(f) show propagation against the wave (towards the equator). In each panel, electrons have the same initial energy, pitch angle and latitude, and the line colors represent the initial uniform sampling in gyrophase. Pairs of dashed lines represent the approximate spatial interval on which the fundamental cyclotron resonance produces strong scattering; for the harmonic resonances $n = \pm 2$, the interval a delimited by dotted lines.

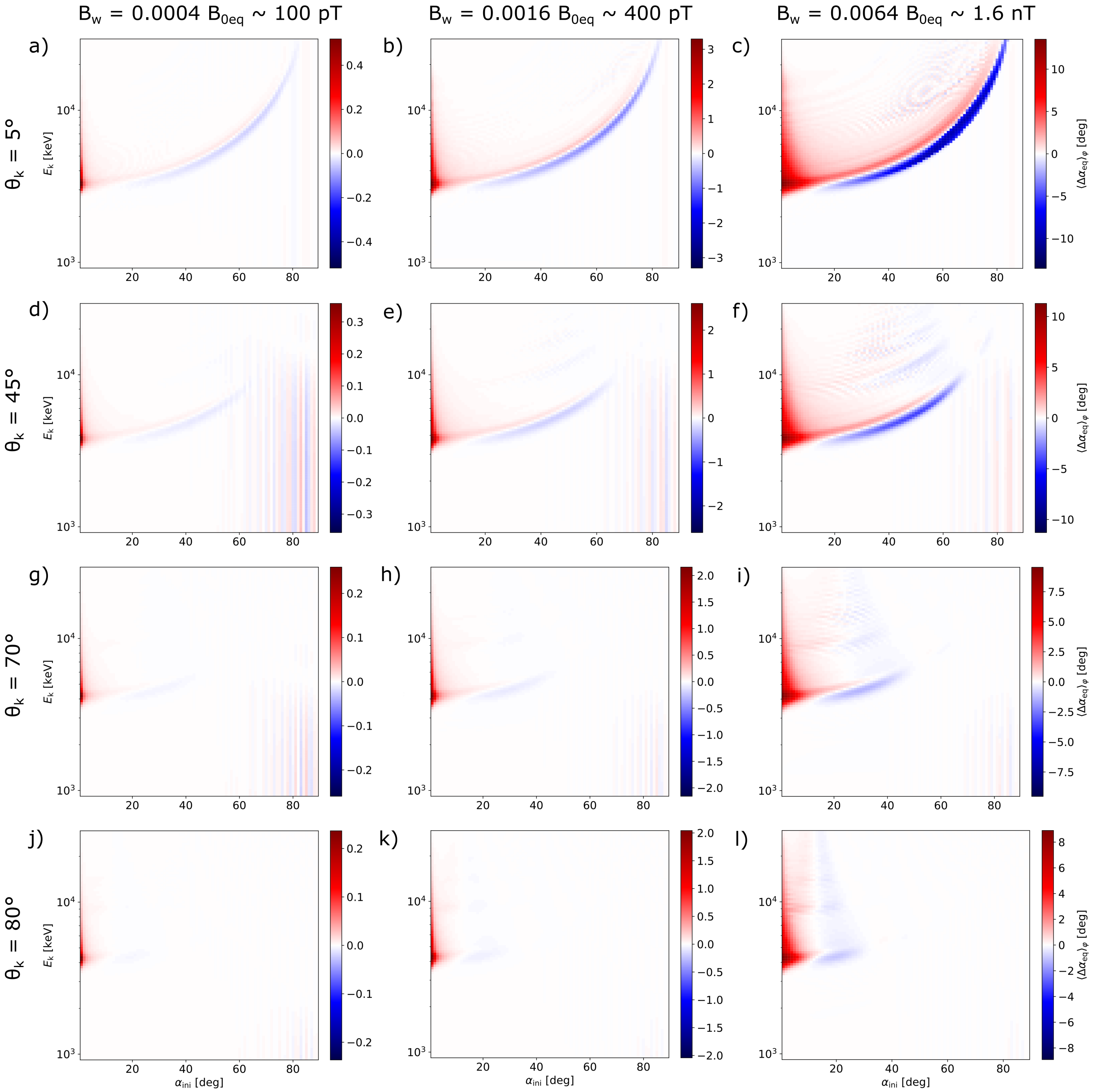

Figure 4. Average change $\langle\Delta\alpha_{\mathrm{eq}}\rangle_\varphi$ in electron equatorial pitch angle for propagation along the EMIC wave packet (stopping point is the end of the wave packet or the mirror point). All particles start at the equator, so the initial pitch angle α_{ini} on the abscissa is equal to the initial α_{eq}. The columns are parametrized by wave amplitude (left to right: $100\,\mathrm{pT}$, $400\,\mathrm{pT}$, and $1.6\,\mathrm{nT}$), and the rows are parametrized by wave normal angle (top to bottom: 5°, 45°, 70°, and 80°). The color bars associated with each panel range from $-\max_{(\alpha_{\mathrm{ini}},E_{\mathrm{k}})}|\langle\Delta\alpha_{\mathrm{eq}}\rangle_\varphi|$ to $+\max_{(\alpha_{\mathrm{ini}},E_{\mathrm{k}})}|\langle\Delta\alpha_{\mathrm{eq}}\rangle_\varphi|$. Vertical stripes at higher pitch angles are related to nonresonant oscillations at mirror points and would disappear after a complete half-bounce.

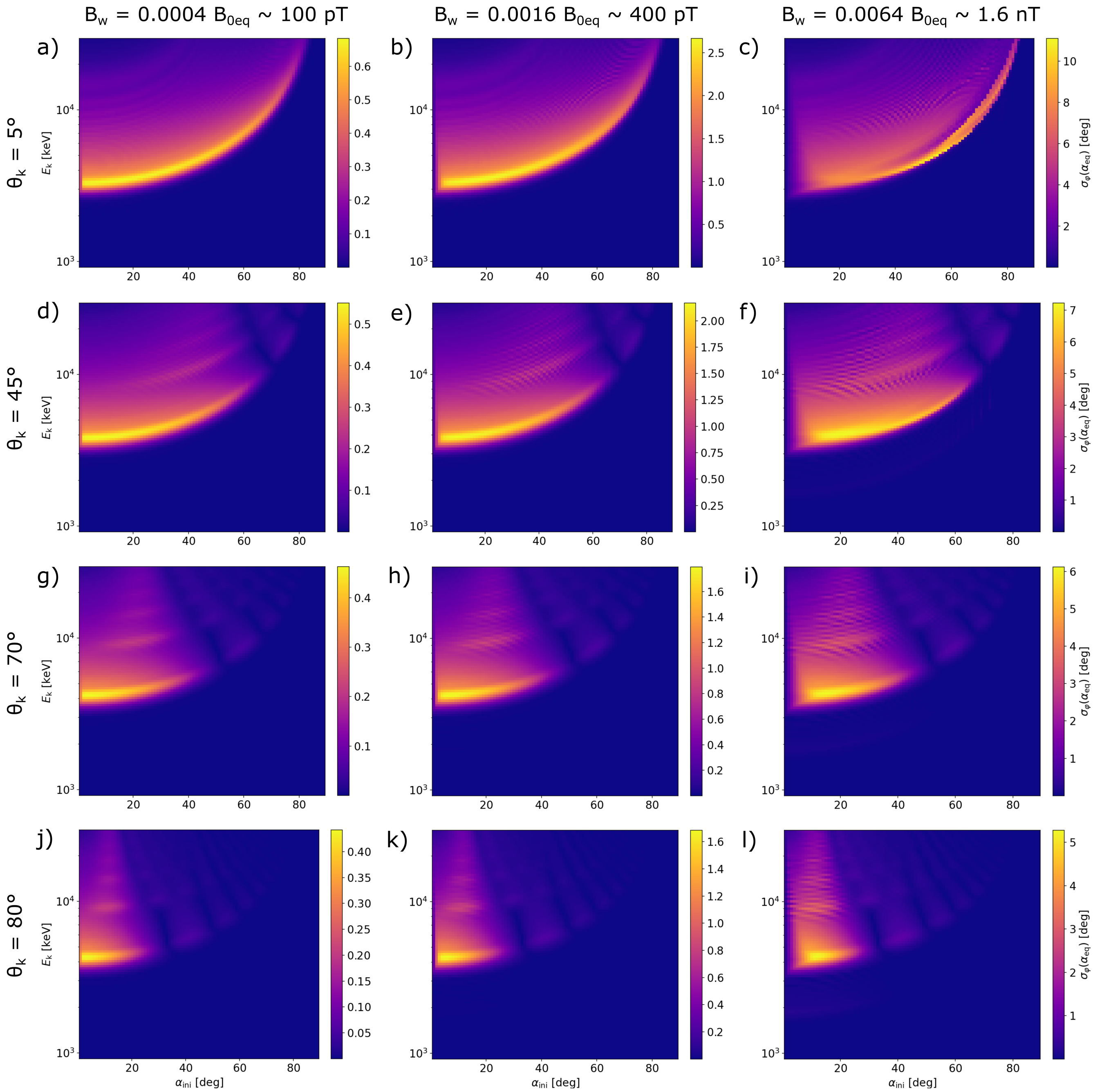

Figure 5. Standard deviation $\sigma_\varphi(\alpha_{\rm eq})$ in electron equatorial pitch angle for propagation along the EMIC wave packet. Same panel format as in Figure 4, but the color bars in each panel now go from 0 to $\max_{(\alpha_{\rm ini},E_{\rm k})}\sigma_\varphi(\alpha_{\rm eq})$.

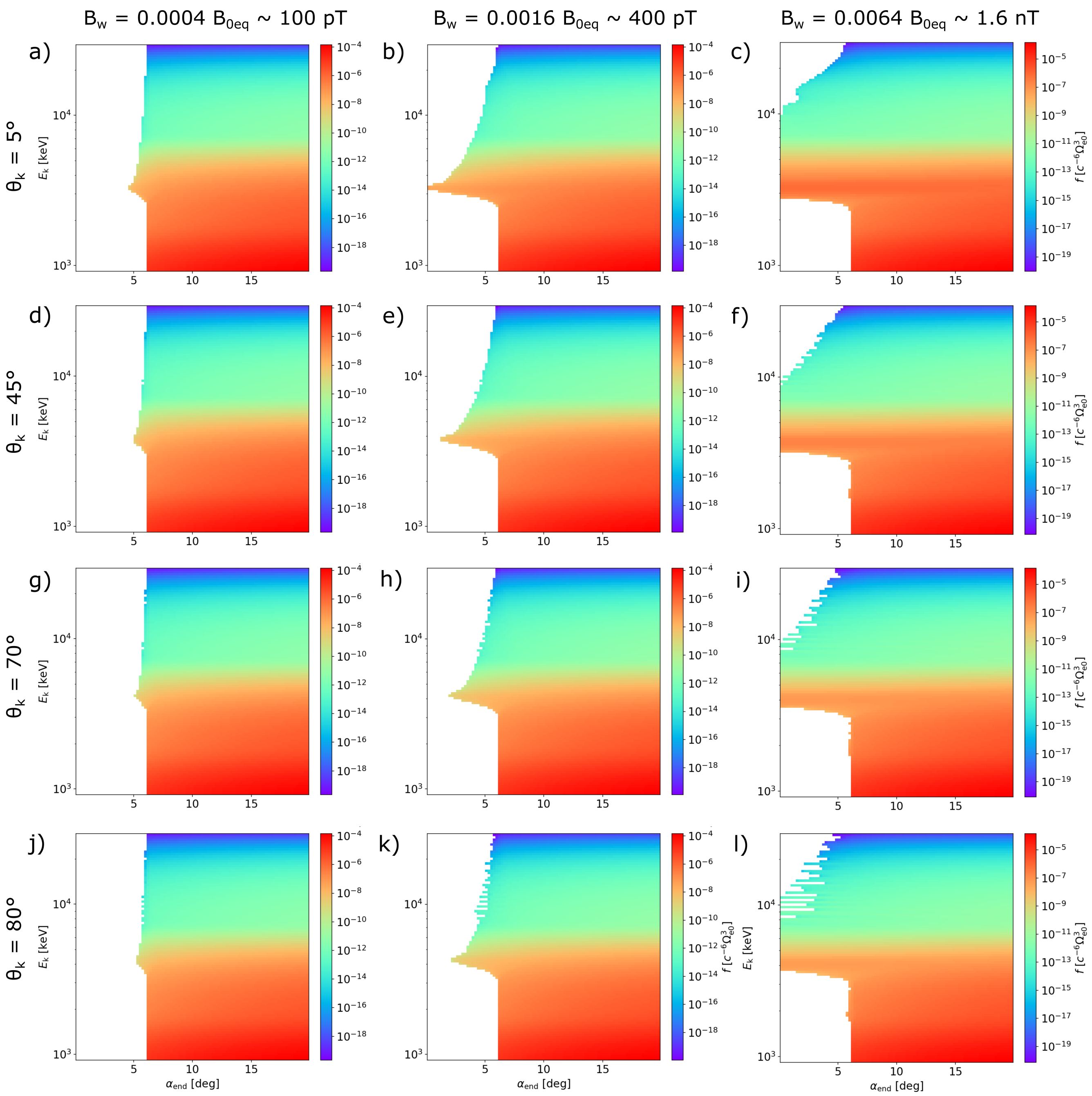

Figure 6. Electron phase space density distribution after resonant interaction with the EMIC wave captured at the end of the wave packet. Range in pitch angles is limited to $0°$–$20°$ to focus on the loss cone. Parametrization of rows and columns follows Figures 4 and 5, but because the co-streaming particles were traced back in time, the pitch angle α_{end} on the abscissa now represents the initial value at the end of the subpacket. The curious small bumps on the boundary between zero and finite PSD values near $2\,\mathrm{MeV}$ in panels (f), (i), and (l) arise due to fractional resonances – see Section 3.3 and Figure 8.

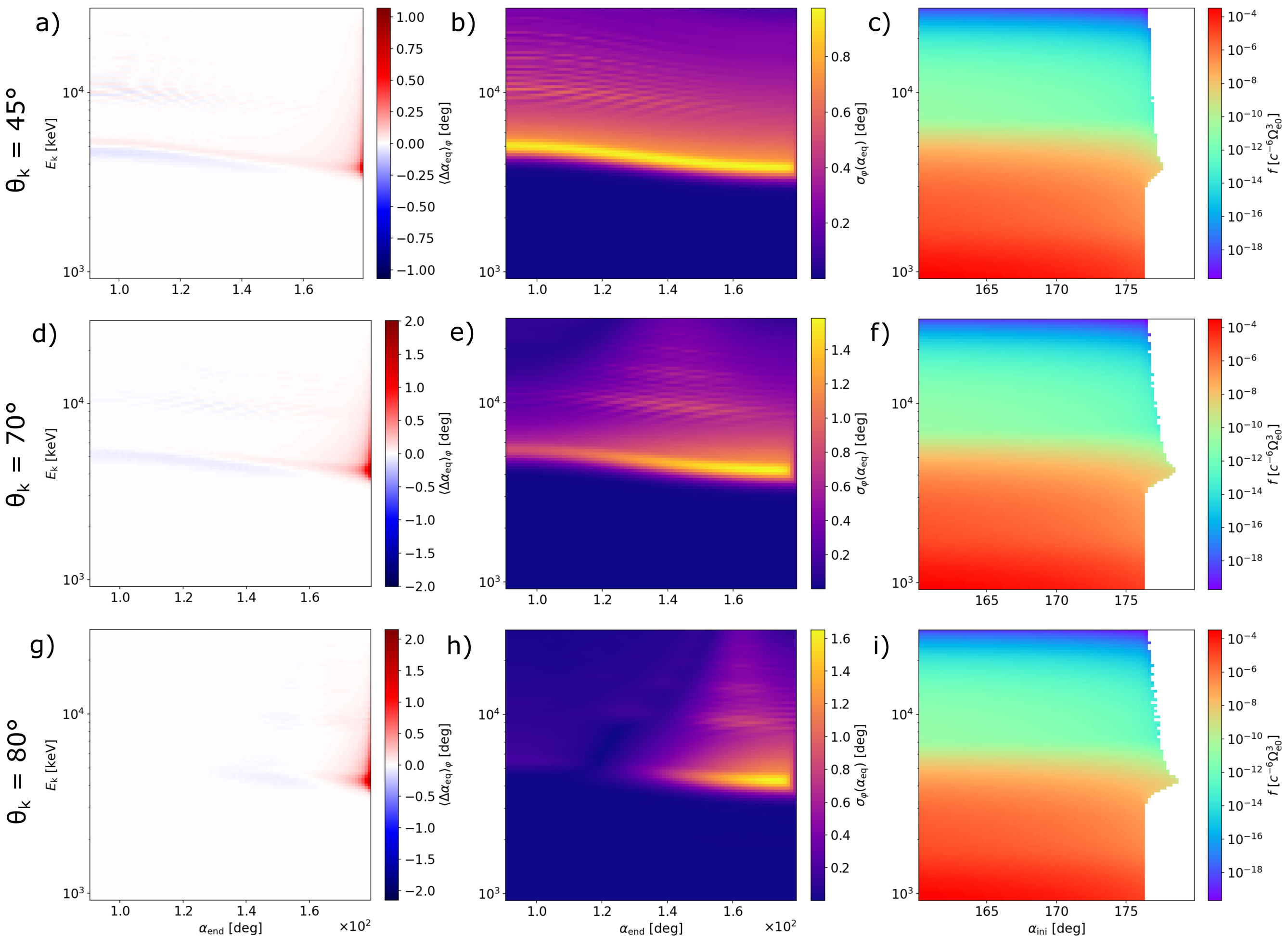

Figure 7. Effect of resonant interactions on electrons propagating against the EMIC wave packet. Panel formatting in the first, second, and third columns follows Figures 4, 5, and 6, respectively. Only a single amplitude value is used, $B_\mathrm{w} = 400\,\mathrm{pT}$, and the wave normal parametrization over rows of panels skips the quasiparallel case $\theta_\mathrm{k} = 5^\circ$, where the resonance effects would be negligible except for extremely ultrarelativistic energies ($E_\mathrm{k} \gtrsim 15\,\mathrm{MeV}$). Note that because the electrons are now counter-streaming, the pitch angles on the abscissas α_ini and α_end were swapped, and particles with initial equatorial pitch angles $> 39^\circ$ are missing from the forward-in-time simulations.

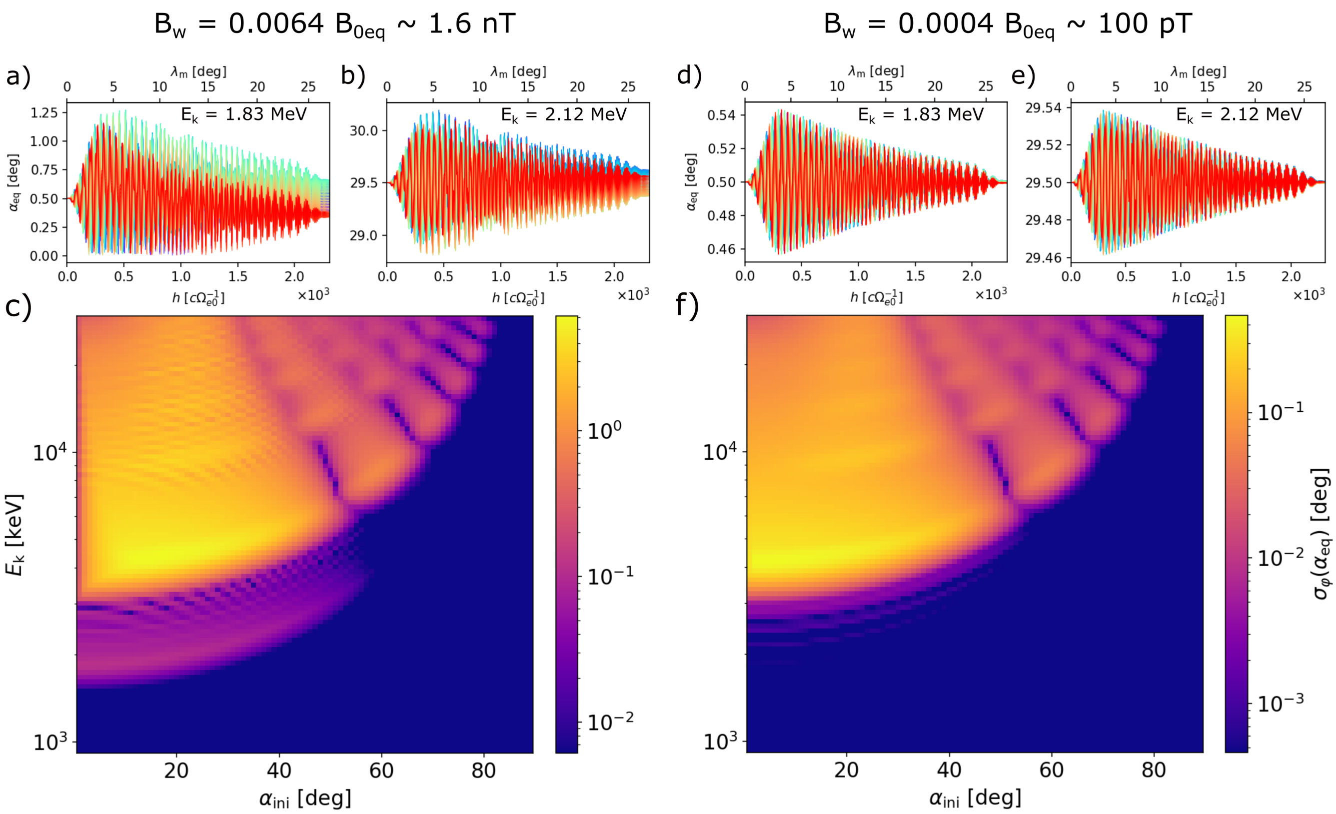

Figure 8. The behavior of fractional resonances explained by particle trajectories and standard deviations in equatorial pitch angle for an EMIC wave with wave normal angle $\theta_{\mathrm{k}} = 70°$. (a),(b) Changes in pitch angle along the field line at energies well below the equatorial fundamental resonance energy $E_{\mathrm{Rmin}} \approx 4\,\mathrm{MeV}$. The wave amplitude is $B_{\mathrm{w}} = 1.6\,\mathrm{nT}$. (c) Standard deviation in equatorial pitch angle plotted in logarithmic scale that spans three orders of magnitude. Weak resonant effects near $2\,\mathrm{MeV}$ become apparent. (d)–(f) Same as (a)–(c), but for a 16 times weaker wave. The resonant effects near $E_{\mathrm{Rmin}}/2$ are now insubstantial compared to the fundamental resonance.